Monthly Notices
of the
ROYAL ASTRONOMICAL SOCIETY

MNRAS **473,** 4003–4020 (2018)
Advance Access publication 2017 October 5

doi:10.1093/mnras/stx2563

Quasar outflows at $z \geq 6$: the impact on the host galaxies

Paramita Barai,[1,2★] Simona Gallerani,[1★] Andrea Pallottini,[1,3,4] Andrea Ferrara,[1] Alessandro Marconi,[5,6] Claudia Cicone,[7] Roberto Maiolino[3,4] and Stefano Carniani[3,4]

[1] *Scuola Normale Superiore, Piazza dei Cavalieri 7, I-56126 Pisa, Italy*
[2] *Instituto de Astronomia, Geofísica e Ciências Atmosféricas, Universidade de São Paulo (IAG-USP), 05508-090, São Paulo, Brazil*
[3] *Cavendish Laboratory, University of Cambridge, 19 J. J. Thomson Ave., Cambridge CB3 0HE, UK*
[4] *Kavli Institute for Cosmology, University of Cambridge, Madingley Road, Cambridge CB3 0HA, UK*
[5] *Dipartimento di Fisica e Astronomia, Universita di Firenze, via G. Sansone 1, I-50019 Sesto Fiorentino (Firenze), Italy*
[6] *INAF – Osservatorio Astrofisico di Arcetri, Largo E. Fermi 5, I-50125 Firenze, Italy*
[7] *INAF – Osservatorio Astronomico di Brera, via Brera 28, I-20121 Milano, Italy*

Accepted 2017 September 27. Received 2017 September 23; in original form 2016 November 28

ABSTRACT

We investigate quasar outflows at $z \geq 6$ by performing zoom-in cosmological hydrodynamical simulations. By employing the smoothed particle hydrodynamics code GADGET-3, we zoom in the $2R_{200}$ region around a $2 \times 10^{12}\,\mathrm{M}_{\odot}$ halo at $z = 6$, inside a $(500\,\mathrm{Mpc})^3$ comoving volume. We compare the results of our active galactic nuclei (AGN) runs with a control simulation in which only stellar/SN feedback is considered. Seeding $10^5\,\mathrm{M}_{\odot}$ black holes (BHs) at the centres of $10^9\,\mathrm{M}_{\odot}$ haloes, we find the following results. BHs accrete gas at the Eddington rate over $z = 9$–6. At $z = 6$, our most-massive BH has grown to $M_{\rm BH} = 4 \times 10^9\,\mathrm{M}_{\odot}$. Fast ($v_{\rm r} > 1000\,\mathrm{km\,s^{-1}}$), powerful ($\dot{M}_{\rm out} \sim 2000\,\mathrm{M}_{\odot}\ \mathrm{yr}^{-1}$) outflows of shock-heated low-density gas form at $z \sim 7$, and propagate up to hundreds kpc. Star formation is quenched over $z = 8$–6, and the total star formation rate (SFR surface density near the galaxy centre) is reduced by a factor of 5 (1000). We analyse the relative contribution of multiple physical process: (i) disrupting cosmic filamentary cold gas inflows, (ii) reducing central gas density, (iii) ejecting gas outside the galaxy; and find that AGN feedback has the following effects at $z = 6$. The inflowing gas mass fraction is reduced by ∼12 per cent, the high-density gas fraction is lowered by ∼13 per cent, and ∼20 per cent of the gas outflows at a speed larger than the escape velocity ($500\,\mathrm{km\,s^{-1}}$). We conclude that quasar-host galaxies at $z \geq 6$ are accreting non-negligible amount of cosmic gas, nevertheless AGN feedback quenches their star formation dominantly by powerful outflows ejecting gas out of the host galaxy halo.

Key words: galaxies: active – galaxies: high-redshift – galaxies: nuclei – quasars: supermassive black holes – early Universe – cosmology: theory.

1 INTRODUCTION

Active galactic nuclei (AGN) are believed to host supermassive black holes (SMBHs) at their centres (e.g. Rees 1984; Kormendy & Richstone 1995; Ferrarese & Ford 2005). The enormous amounts of energy emitted by AGN is generated from accretion of matter on to the SMBHs (e.g. Salpeter 1964; King 2003). Quasars are very powerful AGN existing more commonly at high-z than in the local Universe. Recent observational techniques have started to discover an increasing number of quasars at $z \geq 6$ (e.g. Fan 2006; Mortlock et al. 2011; Venemans et al. 2013; Carnall et al. 2015; Matsuoka et al. 2016). Far-infrared (IR) emission lines, which are unaffected by dust extinction, has lately been proven to be an important tool to probe $z \geq 6$ quasar host galaxies. In particular, the [C II] 158 μm fine structure line (e.g. Maiolino et al. 2005; Walter et al. 2009), and CO emission (e.g. Riechers et al. 2009; Wang et al. 2010; Gallerani et al. 2014; Stefan et al. 2015), from cool atomic and molecular gas (review by Carilli & Walter 2013; Gallerani et al. 2017), are often observed from these high-z sources. The far-IR emission has been modelled in early $z \sim 6$ galaxies using cosmological hydrodynamical simulations (Vallini et al. 2015; Pallottini et al. 2015, 2016).

According to most theoretical and observational studies, feedback from AGN strongly influences the formation and evolution of galaxies, affecting the environment from pc to Mpc scales (e.g. Richstone et al. 1998; Granato et al. 2004; Sazonov et al. 2005; Barai 2008; Fabian 2012; Wagner, Umemura & Bicknell 2013). Cosmological simulations indicate that galaxies build up by the

★ E-mail: paramita.barai@sns.it (PB); simona.gallerani@sns.it (SG)

inflow of cosmic filamentary gas, a fraction of which accretes to the centres feeding and growing the central black holes (BHs), triggering an AGN phase. When the AGN is active for a period of time, its feedback energy output affects the hot/cold gas reservoirs in galaxies by expelling out and heating up some gas, as well as stopping gas inflows, thereby quenching star formation. This limits further gas accretion on to the SMBH, turning the AGN dead. Afterwards with the passage of time, gas might cool and inflow again, feeding the SMBH and triggering another phase of AGN. The result is a self-regulating process, where BHs and host galaxies coevolve during their simultaneous growth. The above processes are regarded to develop correlations in the central BH mass and properties (e.g. stellar mass, stellar velocity dispersion) of the host galaxy, that have been observed (e.g. Magorrian et al. 1998; Silk & Rees 1998; Gebhardt et al. 2000; Shankar et al. 2006; Lyu, Rieke & Alberts 2016).

A strong manifestation of AGN feedback are AGN outflows observed in a wide variety of forms (reviews by Crenshaw, Kraemer & George 2003; Everett 2007). Some examples are blue-shifted broad absorption lines in the ultraviolet and optical (Reichard et al. 2003; Rupke & Veilleux 2011), warm absorbers (Chartas, Brandt & Gallagher 2003; Krongold et al. 2007) and ultrafast outflows in X-rays (Tombesi et al. 2013, 2015), molecular outflows and atomic outflows detected in the IR, submillimetre and millimetre wavelengths (Sturm et al. 2011; Cicone et al. 2014; Dasyra et al. 2015; Feruglio et al. 2015; Morganti et al. 2016), ionized gas in rest-frame optical (Kakkad et al. 2016).

Quasar outflows have also been observed in the early Universe. In the host galaxy of the quasar SDSS J1148+5251 at $z = 6.4$, Maiolino et al. (2012) detected broad wings of the [C II] line tracing a massive outflow with velocities up to $\pm 1300\,\mathrm{km\,s^{-1}}$. Follow-up by Cicone et al. (2015) inferred that the outflow has a complex morphology with the cold gas extended up to 30 kpc, and revised the mass outflow rate lower limit to $1400\,\mathrm{M_\odot\,yr^{-1}}$. The physical mechanisms by which quasar outflows affect their host galaxies remain as open questions.

SMBHs of mass $\geq 10^9\,\mathrm{M_\odot}$ are observed to be in place in luminous quasars by $z \sim 6$, when the Universe was less than 1 Gyr old (e.g. Willott, McLure & Jarvis 2003; Kurk et al. 2007; De Rosa et al. 2014; Wu et al. 2015). It is difficult to understand how these early SMBHs formed over such short time-scales, and there are open issues with various plausible scenarios (e.g. Dijkstra et al. 2008; Mayer et al. 2010; Inayoshi & Omukai 2012; Tanaka & Li 2014; Matsumoto et al. 2015). The presence of massive BH seed candidates ($10^5\,\mathrm{M_\odot}$ at $z > 6$), possibly direct collapse black holes, in a bright Lyman α emitter at $z = 6.6$ have been recently suggested (Smith, Bromm & Loeb 2016; Pacucci et al. 2017).

Concordance galaxy formation models based on cold dark matter (CDM) cosmology widely invoke AGN feedback as a crucial ingredient to self-regulate galaxy and SMBH growth. This has been studied in numerical hydrodynamical simulations (e.g. Di Matteo, Springel & Hernquist 2005; Dubois et al. 2010; Ostriker et al. 2010; Barai, Martel & Germain 2011; Hirschmann et al. 2014), as well as semi-analytical models (e.g. Kauffmann & Haehnelt 2000; Shankar et al. 2004; Bower et al. 2006; Somerville et al. 2008).

AGN feedback should operate mostly in the negative form quenching star formation, as suggested by observations (e.g. Schawinski et al. 2006; Wang et al. 2007; Lanz et al. 2016), and simulations (e.g. Scannapieco, Silk & Bouwens 2005; van de Voort et al. 2011; Dubois et al. 2013; Tremmel et al. 2016). This feedback limits the formation of massive stellar systems, enabling simulations to reproduce the observed exponential cut-off at the bright-end of galaxy luminosity function (e.g. Croton et al. 2006; Silk & Mamon 2012), as opposed to the dark matter (DM) halo mass function. Populations of old, passive (the red and dead) massive elliptical galaxies are observed at $z \sim 2$ (e.g. Cimatti et al. 2004; Saracco et al. 2005; Whitaker et al. 2013). This suggests that quasar feedback was already suppressing star formation at high-z.

At the same time, AGN feedback can occasionally be positive, by inducing star formation, and this aspect also plays an important role. AGN outflows can overpressure and compress clumpy gas clouds, triggering starbursts, as have been shown in theoretical and numerical studies (e.g. De Young 1989; Silk 2005; Zubovas et al. 2013), including cold molecular clumps condensing out in quasar outflows (Ferrara & Scannapieco 2016). Positive feedback has been observed in jet-induced star formation and radio-optical alignment (e.g. Chambers, Miley & van Breugel 1987; Zinn et al. 2013), as well as in Seyfert-like radio-quiet AGN (Cresci et al. 2015).

AGN feedback in high-z galaxies has been probed in a few previous numerical studies. Using zoom-in simulations, Costa et al. (2014) examined the environment of bright quasars at $z \sim 6$ computing the thermal X-ray emission. Furthermore, Costa, Sijacki & Haehnelt (2015) explored fast cold gas (originated by radiative cooling) moving together with the hot bipolar AGN outflows. Richardson et al. (2016) performed zoom simulations of a forming galaxy cluster, and present AGN feedback results at $z = 5$, finding that AGN growth is self-regulated, regardless of Eulerian versus Lagrangian numerical methods used. Bieri et al. (2016) executed radiation-hydrodynamical simulations of idealized gas-rich galaxy discs, where photons from a quasar interacts with the multiphase interstellar medium (ISM), and are found to generate powerful infrared-radiatively-driven outflows. Using a $(400\,h^{-1}\mathrm{Mpc})^3$ cosmological simulation, Waters et al. (2016) predicted the properties of AGN populations at $z = 8$–14, and found $(10^6$–$10^8)\,\mathrm{M_\odot}$ black holes accreting close to their Eddington luminosity.

In this paper, we perform cosmological zoom-in simulations of quasar outflows at $z \geq 6$. Our goals are to investigate the impact of AGN outflows on host galaxies in the early Universe, and compute the outflow properties. We aim to determine the dominant physical mechanism(s) affecting star formation, by examining the relative contributions of (i) halting of cold inflows, (ii) reducing central gas density and hence the mass that can be converted to stars, (iii) ejecting gas outside galaxy. In order to simulate massive quasar-host galaxies within the cosmological context, a large periodic boxsize is needed. At the same time, a low enough gas particle mass is desired, in order to resolve the smaller scale structures. We decide to execute zoomed-in simulations to optimize the computational resource requirements, together with simulating a large cosmological box using the desired resolution.

This paper is organized as follows: we describe our numerical code and simulation setup in Section 2, present and analyse our results in Section 3 and in Section 4 we give a summary of our main findings.

2 NUMERICAL METHOD

We use a modified version of the TreePM (particle mesh) – SPH (smoothed particle hydrodynamics) code GADGET-3 (Springel 2005). It includes an improved version of SPH (Beck et al. 2016) consisting of a higher order Wendland C4 interpolating kernel, a time-dependent artificial viscosity term, and an artificial conduction term. Our simulations are outlined in Section 2.1, and the different runs in Section 2.4.

The physical mechanisms of star formation, supernovae (SN) explosions, gas accretion on to SMBHs and resulting energy feedback

are complex, with the gas motion driven by both thermal and radiation pressure. The relevant physical scales are orders of magnitude below the scales resolved in current galaxy formation simulations. Hence, such physical processes are incorporated in the simulations using subresolution numerical prescriptions (e.g. Springel, Di Matteo & Hernquist 2005). The physics of the gas is modelled using spatially averaged properties describing the medium on scales that are resolved in cosmological simulations. The subresolution physics that we use are described in Section 2.2, with the BH feedback prescriptions detailed in Section 2.3.

2.1 Simulations

We perform zoomed-in cosmological hydrodynamical simulations of high-redshift quasar-host galaxies. The initial conditions are generated using the MUSIC[1] software (Hahn & Abel 2011), following the steps below. A concordance flat ΛCDM model is used, with the cosmological parameters (Planck Collaboration XIII 2015,): $\Omega_{M,0} = 0.3089$, $\Omega_{\Lambda,0} = 0.6911$, $\Omega_{B,0} = 0.0486$, $H_0 = 67.74\,\mathrm{km\,s^{-1}\,Mpc^{-1}}$. We express distances in the comoving scale unless differently stated.

First, a DM only low-resolution simulation is carried out of a $(500\,\mathrm{Mpc})^3$ comoving volume, using 256^3 DM particles. Here, the DM particle mass is $2 \times 10^{10}\,\mathrm{M_\odot}$, and the gravitational softening length is $33\,h^{-1}\,\mathrm{kpc^{-1}}$ comoving. The cosmological box is evolved from $z = 100$ up to $z = 6$, using periodic boundary conditions. Haloes are identified within it using the Friends-of-Friends (FOF) group finder algorithm. We select the most-massive halo at $z = 6$ for the purpose of zoom-in. It has a total mass $M_{\rm halo} = 4.4 \times 10^{12}\,\mathrm{M_\odot}$, and a virial radius $R_{200} \simeq 511\,\mathrm{kpc}$ comoving. The halo mass and virial radius in comoving coordinates (R_{200}) are related such that R_{200} encloses a density 200 times the mean comoving matter density of the Universe:

$$M_{\rm halo} = \frac{4\pi}{3} R_{200}^3 \left(200 \rho_{\rm crit} \Omega_{M,0}\right), \quad (1)$$

where $\rho_{\rm crit} = 3H_0^2/(8\pi G)$ is the present critical density.

We select the DM particles around the most-massive halo, belonging inside a cubic box of side $2R_{200} \simeq 1022\,\mathrm{kpc}$ comoving at $z = 6$. These DM particles are tracked back to our initial condition at $z = 100$, and the Lagrangian region occupied by them is determined. It is a volume of size $(5.21\,\mathrm{Mpc})^3$. The Lagrangian region is populated with particles of higher resolution: DM and baryons, going over 5 further levels of refinement. While the coarser resolution has 8 levels of refinement, the highest resolution has 13 refinement levels.

Finally, we restart a zoom-in simulation of the selected halo containing the high-resolution DM and gas particles ($N_{\rm part} = 2 \times 591\,408$) in the central $(5.21\,\mathrm{Mpc})^3$ region, and the low-resolution ($N_{\rm part} = 17\,224\,370$) DM particles outside the central zoomed region populating the remaining of the $(500\,\mathrm{Mpc})^3$ volume. The high-resolution particle masses are $m_{\rm DM} = 7.54 \times 10^6\,\mathrm{M_\odot}$ and $m_{\rm gas} = 1.41 \times 10^6\,\mathrm{M_\odot}$. We employ $L_{\rm soft} = 1\,h^{-1}\,\mathrm{kpc^{-1}}$ comoving as the Plummer-equivalent softening length for gravitational forces, for these high-resolution DM and gas particles.

We have checked and ruled out any possible contamination by low-resolution particles within the zoomed volume during the simulations. There are no low-resolution DM particles inside a spherical region of radius $2R_{200}$ around the most-massive galaxy centre at each snapshot redshift. We verified this at all of our 37 snapshots distributed between $z = 20$ and $z = 6$. Usually a contamination level of <1 per cent could be allowed in zoom-in simulations.

2.2 Cooling, star formation, SN feedback

Radiative cooling and heating is implemented by adopting the cooling rates from the tables of Wiersma, Schaye & Smith (2009), which includes metal-line cooling. The photoionization code CLOUDY (e.g. Ferland et al. 1998) was used to pre-compute the cooling tables, taking into account the following. Eleven element species (H, He, C, Ca, O, N, Ne, Mg, S, Si, Fe) are tracked, and the gas is assumed to be dust-free, optically thin and in ionization equilibrium. Heating from a spatially uniform time-dependent photoionizing radiation is considered from the cosmic microwave background and the ultraviolet/X-ray background [assuming the Haardt & Madau (2001) model].

Star formation is implemented following the multiphase effective subresolution model by Springel & Hernquist (2003). Gas particles with density above a limiting threshold, $n_{\rm SF} = 0.13\,\mathrm{cm^{-3}}$ (in units of number density of hydrogen atoms), represent regions of the ISM containing cold clouds in pressure equilibrium with hot gas. Collisionless star particles are spawned from these high-density gas particles, based on the stochastic scheme by Katz, Weinberg & Hernquist (1996).

Kinetic feedback from supernovae is included applying the energy-driven wind prescription. The wind mass-loss rate ($\dot{M}_{\rm SN}$) relates to the SF rate ($\dot{M}_\star$) as: $\dot{M}_{\rm SN} = \eta \dot{M}_\star$. We adopt a value for the wind mass loading factor, $\eta = 2$ (e.g. Tornatore et al. 2007; Tescari et al. 2011; Barai et al. 2013), following observations revealing that SN-driven outflow rates in galaxies are comparable to or a few times larger than their SF rates (e.g. Martin 1999; Pettini et al. 2002; Bouche et al. 2012; Newman et al. 2012). The wind kinetic energy is a fixed fraction χ of SN energy: $\frac{1}{2}\dot{M}_{\rm SN} v_{\rm SN}^2 = \chi \epsilon_{\rm SN} \dot{M}_\star$. Here, $v_{\rm SN}$ is the wind velocity, and $\epsilon_{\rm SN} = 1.1 \times 10^{49}\,\mathrm{erg\,M_\odot^{-1}}$ is the average energy released by SN for each $\mathrm{M_\odot}$ of stars formed. We adopt a constant-velocity outflow with $v_{\rm SN} = 350\,\mathrm{km\,s^{-1}}$ (as was done in e.g. Barai et al. 2015; Biffi et al. 2016).

Stellar evolution and chemical enrichment are computed for the 11 elements (following Tornatore et al. 2007). Each star particle is treated as a simple stellar population (SSP). Given a stellar initial mass function (IMF), the mass of the SSP is varied in time following the death of stars, and accounting for stellar mass losses. We include a fixed stellar IMF from Chabrier (2003), in the mass range (0.1–100) $\mathrm{M_\odot}$. Stars within a mass interval [8–40] $\mathrm{M_\odot}$ become SN first before turning into stellar-mass black holes at the end of their lives, while stars of mass $>40\,\mathrm{M_\odot}$ are allowed to directly end in black holes without contributing to enrichment.

Different yields are used from Type Ia SN (Thielemann et al. 2003), Type II SN (Woosley & Weaver 1995), and asymptotic giant branch stars (van den Hoek & Groenewegen 1997). Stellar populations release metals with mass-dependent time delays, employing the lifetime function by Padovani & Matteucci (1993). The mass range for SN-II is $M/\mathrm{M_\odot} > 8$, while that for SN-Ia originating from binary systems is $0.8 < M/\mathrm{M_\odot} < 8$ with a binary fraction of 10 per cent. Both SN-Ia and SN-II also contribute to energy feedback within the chemical evolution model of Tornatore et al. (2007). In addition, there is mass loss through stellar winds and SN explosions, which are self-consistently computed for the given IMF and lifetime function. A fraction of a star particle's mass is restored as

[1] MUSIC–Multiscale Initial Conditions for Cosmological Simulations: https://bitbucket.org/ohahn/music

diffuse gas during its evolution, and distributed to the surrounding gas. The ejected energy (coupled thermally) and enriched material are spread among the neighbouring gas particles with weights given by the SPH kernel.

2.3 BH models

2.3.1 BH seeding

A BH (collisionless sink particle of mass $M_{\rm BH}$) is seeded at the centre of each massive galaxy, whenever it reaches a total mass $M_{\rm halo} > 10^9\,{\rm M}_\odot$, which does not contain a BH already. Haloes are identified by executing a FOF group finder on-the-fly within our simulations. Galaxies are tracked simultaneously using the subhalo finder *SubFind*, which associates substructures to FOF haloes. The centre of each galaxy is considered as the location of the gravitational potential minimum of its subhalo.

The seed BHs have an initial mass $M_{\rm BH} = 10^5\,{\rm M}_\odot$. Such massive seeds correspond to the direct collapse BH formation scenario.

2.3.2 BH accretion

The BHs subsequently grow by accreting surrounding gas and by merger with other BHs. Gas accretion on to a BH is parametrized by the Bondi rate ($\dot{M}_{\rm Bondi}$) and is limited to the Eddington rate ($\dot{M}_{\rm Edd}$),

$$\dot{M}_{\rm BH} = \min\left(\dot{M}_{\rm Bondi}, \dot{M}_{\rm Edd}\right). \tag{2}$$

Here, $\dot{M}_{\rm Bondi}$ is the Bondi–Hoyle–Lyttleton rate (Hoyle & Lyttleton 1939; Bondi & Hoyle 1944; Bondi 1952):

$$\dot{M}_{\rm Bondi} = \alpha \frac{4\pi G^2 M_{\rm BH}^2 \rho}{\left(c_{\rm s}^2 + v^2\right)^{3/2}}, \tag{3}$$

where G is the gravitational constant, ρ is the gas density, $c_{\rm s}$ is the sound speed and v is the velocity of the BH relative to the gas. We set $\alpha = 100$ as a numerical boost factor (as done by e.g. Springel, Di Matteo & Hernquist 2005; Khalatyan et al. 2008; Johansson, Naab & Burkert 2009; Dubois et al. 2013). In equation (2), $\dot{M}_{\rm Edd}$ is the Eddington mass accretion rate expressed in terms of the Eddington luminosity,

$$L_{\rm Edd} = \frac{4\pi G M_{\rm BH} m_{\rm p} c}{\sigma_{\rm T}} = \epsilon_{\rm r} \dot{M}_{\rm Edd} c^2, \tag{4}$$

where $m_{\rm p}$ is the mass of a proton, c is the speed of light and $\sigma_{\rm T}$ is the Thomson scattering cross-section for an electron.

BH accretion is numerically implemented in the GADGET-3 code using a stochastic methodology to *swallow* neighbouring gas particles (originally from Springel, Di Matteo & Hernquist 2005), as described in Barai et al. (2014, 2016).

2.3.3 BH feedback

A fraction of the accreted rest-mass energy is radiated away by each BH. The radiation luminosity is

$$L_{\rm r} = \epsilon_{\rm r} \dot{M}_{\rm BH} c^2, \tag{5}$$

with $\epsilon_{\rm r}$ being the radiative efficiency. We adopt the mean value for radiatively efficient accretion on to a Schwarzschild BH (Shakura & Sunyaev 1973): $\epsilon_{\rm r} = 0.1$. A fraction $\epsilon_{\rm f}$ (feedback efficiency) of this radiated energy is coupled to the surrounding gas as feedback energy:

$$\dot{E}_{\rm feed} = \epsilon_{\rm f} L_{\rm r} = \epsilon_{\rm f} \epsilon_{\rm r} \dot{M}_{\rm BH} c^2. \tag{6}$$

The BH feedback energy is distributed in the *kinetic* form (introduced in Barai et al. 2014, 2016, as energy-driven wind) only, and no thermal feedback is included. Surrounding gas is driven outward at a velocity $v_{\rm w}$ and mass outflow rate $\dot{M}_{\rm w}$. Given the energy-conservation equation,

$$\frac{1}{2}\dot{M}_{\rm w} v_{\rm w}^2 = \dot{E}_{\rm feed} = \epsilon_{\rm f}\epsilon_{\rm r}\dot{M}_{\rm BH} c^2, \tag{7}$$

the outflow rate can be expressed in terms of the BH accretion rate,

$$\dot{M}_{\rm w} = 2\epsilon_{\rm f}\epsilon_{\rm r}\dot{M}_{\rm BH}\frac{c^2}{v_{\rm w}^2}. \tag{8}$$

The free parameter $\epsilon_{\rm f}$ is usually calibrated to fit the correlation between central BH mass and host galaxy stellar velocity dispersion observed in the local Universe (e.g. Di Matteo et al. 2008; Rasia et al. 2015, in cosmological simulations using thermal AGN feedback models).

Here, we use the parameter values: $\epsilon_{\rm f} = 0.05$ and $v_{\rm w} = 10\,000\,{\rm km\,s^{-1}}$. The wind kick velocity ($v_{\rm w}$) was first chosen motivated by typical AGN wind velocities seen in observations of a few 1000 to $10\,000\,{\rm km\,s^{-1}}$ (e.g. Ramirez 2008; Perna et al. 2015; Williams et al. 2016). Keeping $v_{\rm w}$ fixed, we then selected the value of $\epsilon_{\rm f}$, because this parameter set was obtained as one to provide a closest match of the simulation versus observational [$M_{\rm BH}$–$\sigma_\star$] relation (Barai et al. 2014), using the same kinetic AGN feedback model.

The implementation of the BH subresolution models in the GADGET-3 code involves computing physical quantities by kernel-weighted smoothing over gas particles neighbouring each BH. The relevant kernel size, or the BH smoothing length $h_{\rm BH}$, is determined at each time-step (analogous to finding gas particle smoothing length) by implicit solution of the equation,

$$\frac{4}{3}\pi h_{\rm BH}^3 \rho_{\rm BH} = M_{\rm ngb}, \tag{9}$$

where $\rho_{\rm BH}$ is the kernel estimate of the gas density at the position of the BH, and $M_{\rm ngb}$ is the mass of 200 neighbouring gas particles (same number of neighbours as for SPH). The numerical value of $h_{\rm BH}$ is inversely proportional to the density of gas in the immediate environment of a BH. BHs that lie at galaxy centres have a smaller $h_{\rm BH}$ than off-centre BHs, because gas density within a galaxy peaks at the centre. In our simulations, $h_{\rm BH}$ typically lies between (1 and 20) h^{-1} kpc, with an average value of $2\,h^{-1}$ kpc. The minimum value of $h_{\rm BH}$ is comparable to the gravitational softening length of the gas particles. Further details of $h_{\rm BH}$ can be found in Appendix A.

The kinetic feedback energy from each BH is distributed to the gas within a distance $h_{\rm BH}$, lying inside a volume of a pre-defined geometry: bi-cone, or sphere. For the bi-cone geometry, two conical volumes are defined with the BH at the apex, and the cones along two diametrically opposed directions. The slant height of each cone is $h_{\rm BH}$, and the half-opening angle is taken as 45°. The cone-axis direction is considered as fixed for each BH. A fixed direction is randomly assigned to a BH in our simulations during its seeding at the halo centre. For the sphere geometry, the radius is $h_{\rm BH}$ (this case is equivalent to a bi-cone with a half-opening angle of 90°).

Gas particles lying within the pre-defined geometry are tracked, and their total mass $M_{\rm gas}^{\rm vicinity}$ is computed. These gas particles are stochastically selected and kicked into AGN wind, by imparting a one-time $v_{\rm w}$ velocity boost. We use a probabilistic criterion, similar

to other subresolution prescriptions in GADGET-3. The probability for ith gas particle within the volume to be kicked is calculated as

$$p_i = \frac{\dot{M}_{\rm w}\Delta t}{M_{\rm gas}^{\rm vicinity}}, \quad (10)$$

where Δt is the time-step and $\dot{M}_{\rm w}$ is the mass outflow rate obtained from equation (8). At a given time-step, all the gas particles within the pre-defined geometry have the same probability to be ejected. The inverse proportionality of p_i with $M_{\rm gas}^{\rm vicinity}$ ensures that the number of particles kicked does not depend on the geometry of the volume, but depends on $\dot{M}_{\rm w}$ only. The quantity $\dot{M}_{\rm w}\Delta t$ is the mass of gas to be kicked. The probability p_i is constructed such that the available gas particles (total mass $M_{\rm gas}^{\rm vicinity}$ within pre-defined geometry) are sampled to reproduce kicking at the rate given by $\dot{M}_{\rm w}$, on average.

A random number x_i, uniformly distributed in the interval [0, 1], is drawn and compared with p_i. For $x_i < p_i$, the gas particle is given an AGN wind kick, such that its new velocity becomes

$$\vec{v}_{\rm new} = \vec{v}_{\rm old} + v_{\rm w}\hat{n}. \quad (11)$$

The kick direction $\hat{n}$ is set radially outward from the BH.

In this work, we consider only two geometries of the region where BH feedback energy is distributed: bi-conical and spherical. This is to bracket the range of physical processes happening in the real Universe, where AGN feedback is observed to operate anisotropically in complex manners. For simplicity, we chose a specific bi-cone for each BH, which should capture the main difference between bi-conical and spherical cases. Another possibility is to consider variations of the direction (and opening angle) of the bi-conical feedback, depending on neighbouring gas angular momentum or BH spin. This requires additional simulations and specific comparison with observations to distinguish between the physical scenarios and forms prospects for future work.

2.3.4 BH reposition

We incorporate a scheme for BH repositioning or *pinning* (also done in e.g. Springel, Di Matteo & Hernquist 2005; Sijacki et al. 2007; Booth & Schaye 2009; Ragone-Figueroa et al. 2013; Wurster & Thacker 2013; Schaye et al. 2015). It is often denoted in the literature as the BH advection algorithm. Each BH is repositioned manually at each time-step to the centre (minimum gravitational potential location) of its host galaxy. This is done to correct for dynamical movements of BH particles wandering away from galaxy centres by numerical effects in SPH simulations. We perform one run without BH repositioning, and its implications are discussed in Section 3.

However, the BH advection algorithm has its limitations. It fails to capture the Gyr time-scale of sinking orbits for BHs during galaxy mergers (e.g. Governato, Colpi & Maraschi 1994). It results in a nearly immediate SMBH merger, as well as high BH accretion rates during merger events. As an improvement, Tremmel et al. (2015, 2016) proposed a subgrid force correction term to model the dynamical friction of an SMBH as it orbits within its host galaxy. This new approach allows for long-lived dual SMBH orbits during a galaxy merger, and accurately follows an SMBH's gradual orbital decay.

2.3.5 BH merging

We assume that central BHs merge when their host galaxies merge during hierarchical structure formation. When two BH particles come near such that the distance between them is smaller than the smoothing length of either one, and their relative velocity is below the local sound speed, they are allowed to merge to form a single BH (e.g. Sijacki et al. 2007; Di Matteo et al. 2012).

2.4 Series of simulation runs

We execute a series of four simulations, with characteristics listed in Table 1. All the four runs incorporate metal cooling, chemical enrichment, SF and SN feedback. The first run has no AGN included, while the latter three explore different AGN feedback models:

(i) *noAGN* – No BH present. This is a control simulation in which only cooling, enrichment, star formation and SN feedback are implemented.
(ii) *AGNoffset* – With AGN accretion, growth and feedback. Kinetic BH feedback distributed inside bi-cone (45° half opening angle).
(iii) *AGNcone* – Repositioning of BH to halo centre. Kinetic feedback distributed in bi-cone (45° half opening angle).
(iv) *AGNsphere* – Repositioning of BH. Kinetic feedback distributed in sphere (90° half opening angle).

The zoomed-in halo evolves differently in the four runs because of the different feedback models. The precise value of total halo mass ($M_{\rm halo}$) at $z = 6$ is mentioned in the last column of Table 1.

3 RESULTS AND DISCUSSION

3.1 Black hole environment

The spatial locations of the BHs within our *AGNcone* simulation box can be visualized in Fig. 1, overplotted with the gas overdensity. The plotted region is centred on the most-massive galaxy at $z = 6$. The six panels present six redshifts, each one showing a projected $(2000\ {\rm kpc\,h})^3$ comoving volume. The red plus symbols designate BH positions, where the symbol size is proportional to BH mass going from $M_{\rm BH} = 5 \times 10^5\ {\rm M}_\odot$ (smallest symbols in every panel) to $4 \times 10^9\ {\rm M}_\odot$ (largest symbol in the bottom-right panel). The black dashed circle is the virial radius R_{200} of the most-massive galaxy at each epoch plotted.

The earlier epochs ($z = 10, 9, 8$) show BHs being seeded at the centres of galaxies with $M_{\rm halo} > 10^9\ {\rm M}_\odot$. These massive BH-host

Table 1. Simulation runs and parameters.

Run name	AGN feedback algorithm	Reposition of BH to potential minimum	Geometry of region where feedback energy is distributed	Half opening angle of effective cone	Total mass of zoomed-in halo at $z = 6$
noAGN	No BH	–	–	–	$2.4 \times 10^{12}\ {\rm M}_\odot$
AGNoffset	Kinetic	No	Bi-cone	45°	$2.4 \times 10^{12}\ {\rm M}_\odot$
AGNcone	Kinetic	Yes	Bi-cone	45°	$1.6 \times 10^{12}\ {\rm M}_\odot$
AGNsphere	Kinetic	Yes	Sphere	90°	$2.1 \times 10^{12}\ {\rm M}_\odot$

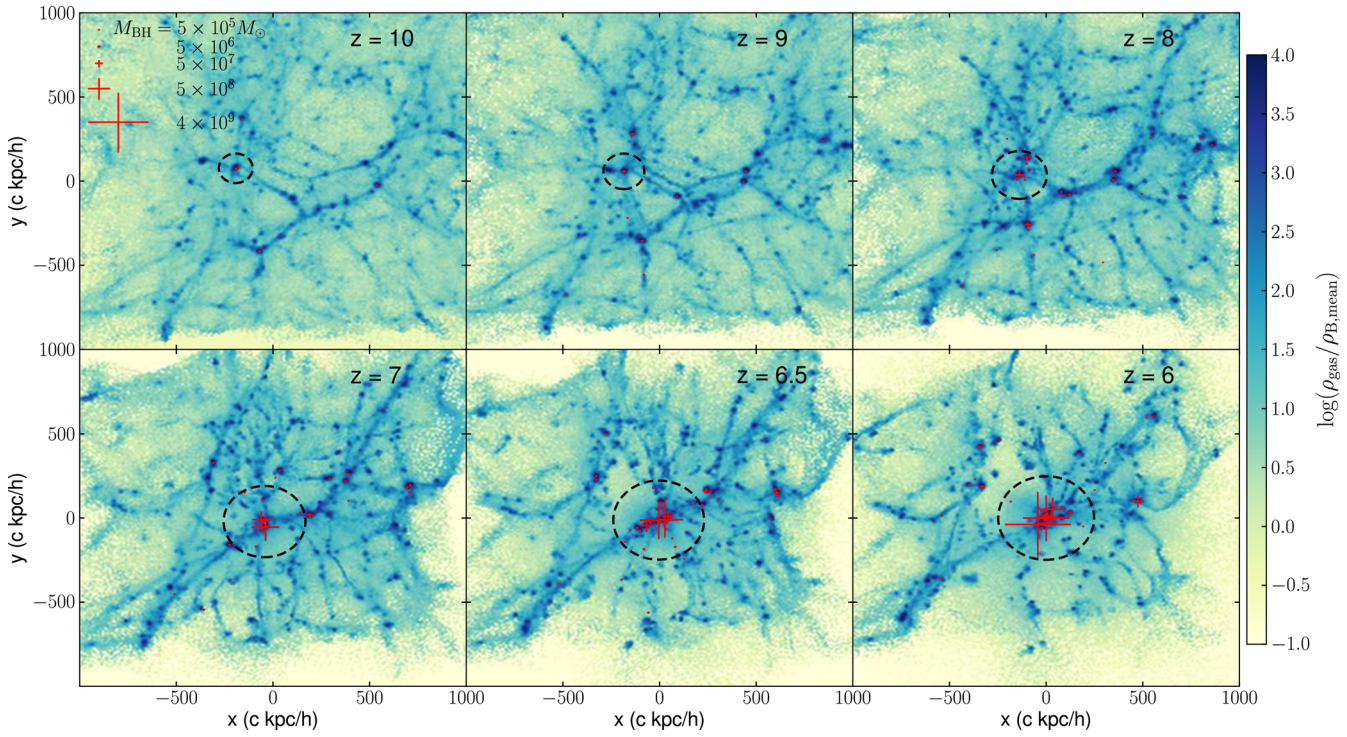

Figure 1. Gas overdensity in the run *AGNcone* at six epochs $z = 10, 9, 8, 7, 6.5, 6$. Each panel shows a projected $(1000\,h^{-1}\,\mathrm{kpc})^3$ comoving volume around the location of the most-massive galaxy at $z = 6$. The red plus symbols designate positions of BHs, with the symbol size proportional to BH mass as indicated in the legend of top-left panel. The largest symbol (bottom-right panel) corresponds to $M_{BH} = 4 \times 10^9\,M_\odot$, and the smallest symbols (every panel) correspond to $M_{BH} = 5 \times 10^5\,M_\odot$. The black dashed circle is the virial radius R_{200} of the most-massive galaxy at each epoch plotted.

galaxies lie at the high-density intersections of cosmological large-scale-structure filaments. When two massive galaxies merge during hierarchical structure formation, their central BHs merge as well (according to the prescription in Section 2.3.5) to form a single larger BH. In addition, the BHs grow in mass by accreting gas from their surroundings, as galaxies evolve and gas inflows to their centres. The later epochs ($z = 6.5, 6$) display a few BHs which have grown supermassive located near the centre of the plotted region.

Initially, the most-massive BH is seeded and grows in the most-massive galaxy, as seen in the top panels of Fig. 1 ($z = 10, 9, 8$). At the later epochs ($z = 7, 6.5, 6$, bottom panels), there is an offset between the most-massive galaxy centre and the most-massive BH location. This is because of the difference of the rates at which a BH and its host galaxy grows in mass. Neighbouring galaxies evolve at different rates, and the galaxy halo which grows to become most massive in the simulation is not the one hosting the most-massive BH, but somewhat offset from it.

We find that in our simulations the BHs form an SMBH binary or triplet (in this run *AGNcone*) at the halo centre, and form a merging system at $z = 6$. This is a physically plausible scenario since binary SMBHs are observed in the local Universe (e.g. Ju et al. 2013; Andrade-Santos et al. 2016). Recent studies have started to observe that quasars often occur in merging systems at high-z. For example, at $z = 4.8$, 50 per cent of quasar host galaxies (3 out of 6) analysed by Trakhtenbrot et al. (2017) are found to have companion submillimetre galaxies.

However, binary SMBHs at $z \geq 6$ have not been detected so far. This discrepancy could be because of limitations of current observations; for example angular resolution being too low and not sufficient to distinguish multiple sources, or BHs being highly obscured and not visible at optical/ultraviolet wavelengths. Thus, our prediction that SMBHs may occur as binaries at $z = 6$–7 makes the case stronger for future observational programs to detect them.

3.2 Black hole accretion and growth

We find that first BHs are seeded at $z \sim 15$ in our simulations, when the first haloes reach $M_{halo} = 10^9\,M_\odot$. In the runs *AGNcone* and *AGNsphere*, one of these first seeds grow to become the most-massive BH. However in run *AGNoffset*, the BH which becomes most massive is seeded at $z \sim 10$. This variance in the seed epochs is because of the different BH growth modes, as described next.

The redshift evolution of the most-massive BH in the three AGN runs is plotted in Fig. 2: BH mass in the top-left panel, BH mass accretion rate ($\dot{M}_{BH}$) at the top-right and Eddington ratio $= \dot{M}_{BH}/\dot{M}_{Edd}$ at the bottom-right panel. Each BH starts from an initial seed of $M_{BH} = 10^5\,M_\odot$, at $z \sim 14$ in the runs *AGNcone* and *AGNsphere* ($z \sim 10$ in *AGNoffset*). The subsequent growth is due to merger with other BHs (revealed as vertical rises in M_{BH}), and gas accretion (visualized as the positive-sloped regions of the M_{BH} versus z curve).

The dominant mode of BH growth occurs over the redshift range $z = 9$–6 in runs *AGNcone* and *AGNsphere*, corresponding to Eddington-limited gas accretion where Eddington ratio =1. The $\dot{M}_{BH}$ has a power-law increase, and the BH mass increases by a factor $\sim 10^3$. The final properties reached at $z = 6$ depends on the simulation: $M_{BH} = 4 \times 10^9\,M_\odot$ and $\dot{M}_{BH} = 100\,M_\odot\,\mathrm{yr}^{-1}$ in run *AGNcone* (red curve), $M_{BH} = 4 \times 10^8\,M_\odot$ and $\dot{M}_{BH} = 6\,M_\odot\,\mathrm{yr}^{-1}$ in run *AGNsphere* (green curve), $M_{BH} = 10^6\,M_\odot$ and $\dot{M}_{BH} < 10^{-5}\,M_\odot\,\mathrm{yr}^{-1}$ in run *AGNoffset* (violet curve). There is variability of the $\dot{M}_{BH}$, whereby it fluctuates by a factor of up to 100.

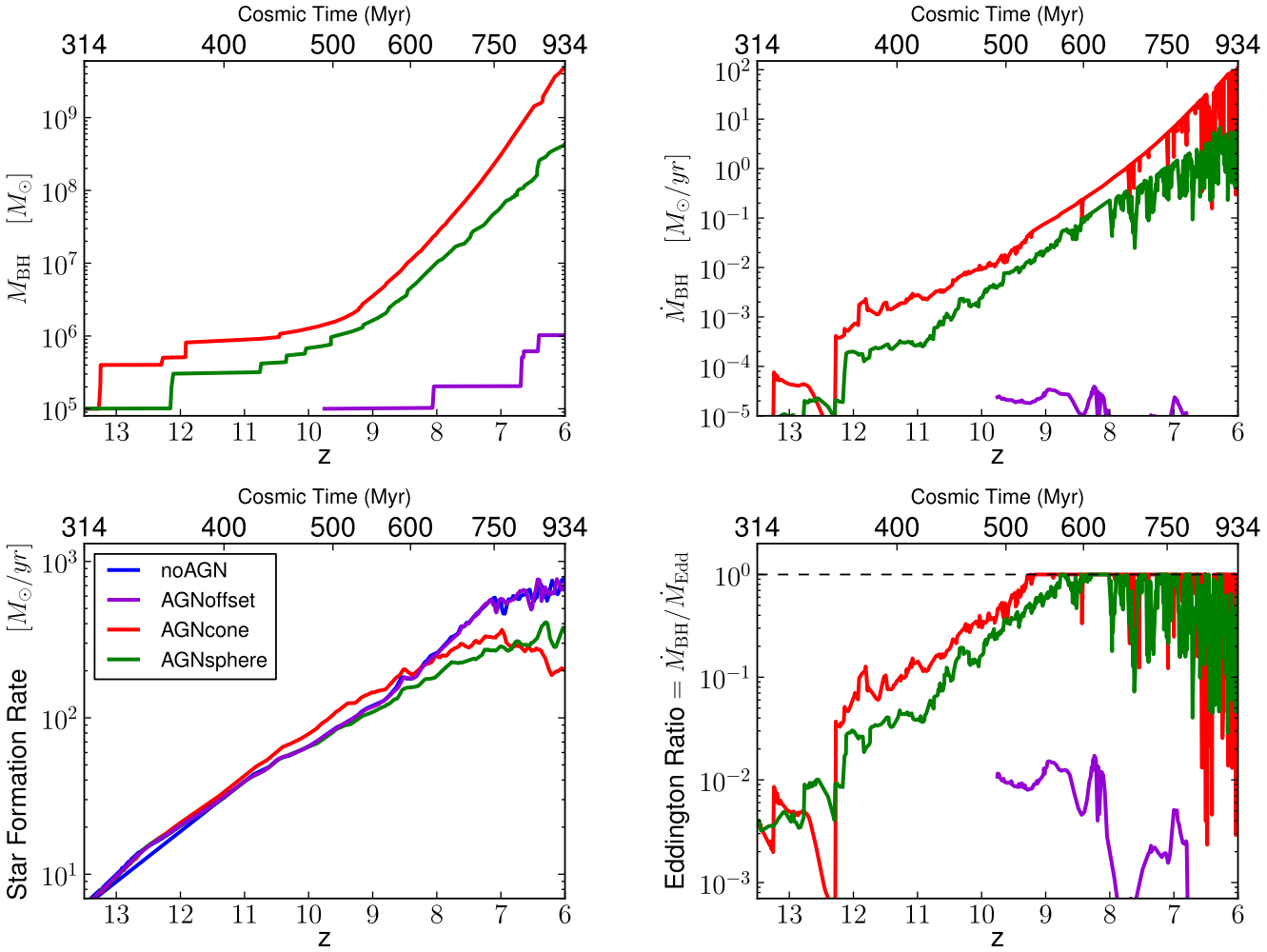

Figure 2. Evolution with redshift of BH mass (top-left panel), mass accretion rate (top-right) and Eddington ratio (bottom-right) of the most-massive BH in each run. The star formation rate (total in whole simulation box) is plotted in the bottom-left panel. The different colours discriminate the runs as labelled in the bottom-left.

The BH grows 10 times more massive at $z = 6$ in the *AGNcone* case than in the *AGNsphere* run. This is because more gas can inflow along the perpendicular direction to the bi-cone, and accrete on to the BH. As discussed later in Section 3.5, the relative direction of the cosmic gas feeding the galaxy (and consequently its central BH) from the large-scale structures remains the same in all the runs. In the *AGNcone* case, a strong outflow develops perpendicular to this direction of cosmic gas infall (Fig. 5). Thus, more gas from the cosmic large-scale structures continue to infall on to the BH and causes it to grow larger.

Our results of early SMBH growth are consistent with previous zoom-in cosmological simulations of high-z quasars. Sijacki, Springel & Haehnelt (2009) found that, starting from seeds of $10^5\,M_\odot$ around $z = 15$ in DM haloes of mass 10^9–$10^{10}\,M_\odot$, it is possible to build up SMBHs of $10^9\,M_\odot$ by $z = 6$ that assemble most of their mass during extended Eddington-limited accretion periods. Costa et al. (2014) identified that the above is true only in the most-massive haloes located in the most-overdense regions. We zoomed-in just the most-massive halo from our parent $(500\,\mathrm{Mpc})^3$ box, where we find BHs growing to $\sim 10^9\,M_\odot$ by $z = 6$. However, our BHs undergo Eddington-limited accretion up to later epochs ($z = 6$) as compared to Costa et al. (2014), who analysed that accretion becomes limited by AGN feedback by $z \sim 9$–8.

We find that the BHs become supermassive ($M_{BH} \sim 10^9\,M_\odot$) in the simulations (*AGNcone* and *AGNsphere*) with BH repositioning, where a BH is repositioned to the centre of its host galaxy. Instead in the case without BH repositioning (run *AGNoffset*, violet curve), the most-massive BH grows up to $10^6\,M_\odot$ only, and the growth is dominated by mergers, since gas accretion is always occurring at low Eddington ratios ($\dot{M}_{BH}/\dot{M}_{Edd} \leq 0.02$). This is because with no repositioning algorithm, a BH is offset from the centre of its host galaxy. Hence, the gas density in the BH vicinity is lower than the case where a BH lies at the galaxy centre with a high gas density. This causes a smaller Bondi accretion rate $\dot{M}_{Bondi}$ (see equation 3), resulting in a tiny BH growth. Therefore, implementing BH repositioning is necessary for our BHs to encounter galaxy-central high-density gas, and accrete at the Eddington rate in order to reach $10^9\,M_\odot$ by $z = 6$.

3.3 Star formation

Stars form in the simulation volume from cold dense gas. The star formation rate (total in the whole simulation box) versus redshift of the four simulations is displayed in Fig. 2, bottom-left panel. The star formation rate (SFR) rises with time in all the runs initially, and continues to increase in the *noAGN* case without a BH. The SFR in

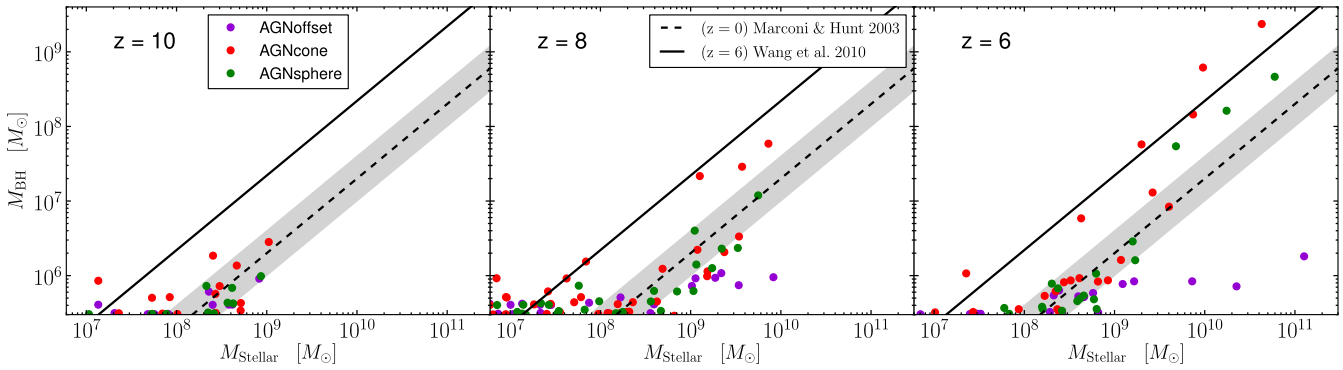

Figure 3. BH mass versus stellar mass of all the galaxies within the zoomed-in volume, at three epochs $z = 10$, 8, 6, in the panels from left. The plotting colour distinguish results from different runs: *AGNoffset* – violet, *AGNcone* – red, *AGNsphere* – green. The black lines indicate the observed BH mass versus stellar bulge mass relation of: local galaxies (Marconi & Hunt 2003) as the dashed line, and $z \sim 6$ quasars (Wang et al. 2010) as the solid line.

run *AGNoffset* is almost similar to that in the run *noAGN*, because the BHs are too small there to generate enough feedback. A similar outcome happens in the runs *AGNcone* and *AGNsphere* at $z \geq 8$, when the BHs are too small.

The star formation mostly occurs over an extended region at galaxy centres, where cosmic large-scale-structure gas inflows and cools. The presence of a BH quenches star formation. We quantify and discuss later in Section 3.7 the details of the SF quenching mechanisms.

The models suppress SF substantially from $z \sim 8$ onwards, when the BHs have grown massive and generate larger feedback energy. Thus, we find that BHs need to grow to $M_{\rm BH} > 10^7\,{\rm M}_\odot$, in order to suppress star formation, even in massive galaxies (of $M_\star = 4 \times 10^{10}\,{\rm M}_\odot$ and specific-SFR $= 5 \times 10^{-9}\,{\rm yr}^{-1}$). BH feedback causes a reduction of SFR up to four times at $z = 6$: from $800\,{\rm M}_\odot\,{\rm yr}^{-1}$ in the *noAGN* run, to $200\,{\rm M}_\odot\,{\rm yr}^{-1}$ in run *AGNcone* and $350\,{\rm M}_\odot\,{\rm yr}^{-1}$ in run *AGNsphere*.

3.4 Black holegalaxy correlation

The BH–galaxy correlation obtained in our simulations is presented in Fig. 3 as the $M_{\rm BH}$ versus $M_\star$ (stellar mass) diagram. We define galaxy stellar mass as the mass of all star particles inside the subhaloes obtained by the subhalo finder *SubFind* (our halo tracking algorithm has been described in Section 2.3). It shows all the galaxies within the zoomed-in volume, at three epochs $z = 10$, 8, 6, in the panels from left. The plotting colour distinguishes results from different runs: *AGNoffset* – violet, *AGNcone* – red, *AGNsphere* – green. Observational data are overplotted as the black lines indicating the BH mass versus stellar bulge mass relationships at different epochs. Local galaxies ($z = 0$) fit the black-dashed line: $M_{\rm BH}/M_\star = 0.002$ (Marconi & Hunt 2003). The ratio is observed to be steeper at high-z. Far-IR and CO bright $z \sim 6$ quasars lie along the black-solid line: median $M_{\rm BH}/M_\star = 0.022$ (Wang et al. 2010). In our run *AGNoffset*, where the most-massive BH reaches $M_{\rm BH} \sim 10^6\,{\rm M}_\odot$ only, the $[M_{\rm BH}$–$M_\star]$ correlation is not reproduced.

Our simulations (runs *AGNcone* and *AGNsphere*) show that, at $z \sim 6$ massive galaxies ($M_\star > 10^9\,{\rm M}_\odot$) contain SMBHs ($M_{\rm BH} > 10^7\,{\rm M}_\odot$) more massive than expected from the local relation. This suggests that SMBHs grow faster than their host galaxies in the early Universe. Observations inferring the $[M_{\rm BH}$–$M_\star]$ correlation in ultraluminous $z \sim 6$ quasars (e.g. Walter et al. 2004; Venemans et al. 2016; Wang et al. 2016) also points to the same scenario. Though it should be noted that, at high-z there are large uncertainties in quantifying the host galaxy stellar masses (e.g. Valiante et al. 2014), which is usually estimated using the dynamical gas mass measured from CO and [C II] observations.

We also see a dependence on the BH mass: less-massive BHs lie on the local relation, albeit with a large scatter; while they *migrate* to the $z = 6$ correlation as they grow. We find the limiting mass as $M_{\rm BH} \sim 10^7\,{\rm M}_\odot$, below which our results more closely match the observed $[M_{\rm BH}$–$M_\star]$ relation at $z = 0$. While at $M_{\rm BH} > 10^7\,{\rm M}_\odot$, the simulated galaxies more closely match the observed correlation at $z = 6$. Such a trend is consistent with observations (e.g. Willott, Bergeron & Omont 2015; Wang et al. 2016), where however the limiting BH mass is 10 times higher: most of the $z \sim 6$ quasars with $M_{\rm BH} \sim 10^8\,{\rm M}_\odot$ are close to the local relationship, while more-massive quasars tend to lie above.

The right-hand panel of Fig. 4 shows the redshift track of the BH mass versus host galaxy stellar mass of the most-massive BH progenitor (which was plotted in Fig. 2). For each curve, the redshifts start from $z = 12$ (bottom-left point), and go up to $z = 6$ (top-left point). The red and green curves indicate that as BHs grow from 10^7 to $10^8\,{\rm M}_\odot$, they migrate from the $z = 0$ to the $z = 6$ correlation. The corresponding redshift evolution of the host galaxy stellar mass of the same BH is shown in the left-hand panel of Fig. 4.

3.5 Gas outflows

While the BHs output feedback energy (Section 2.3), high-velocity gas propagates radially outward and shocks with the surrounding slower moving gas. This creates bubble-like gas outflows originating from the central BH.

3.5.1 Outflow morphology

The outflow morphology is plotted in Fig. 5, which displays the projected gas kinematics in a $(1000\,h^{-1}\,{\rm kpc})^3$ comoving volume in three runs, at $z = 6$. The overdensity, temperature, SFR, carbon abundance ($Z_{\rm C}$) and radial velocity ($v_{\rm r}$) of the gas is plotted in the five rows from the top. We analyse the abundance of carbon, which is one of the most-abundant heavy element in the Universe. Observationally, the [C II] line can be used to characterize the ISM of galaxies, and CO emission can be used to track molecular outflows. We compute $Z_{\rm C}$ as the ratio of carbon mass to the total gas mass for each gas particle. Abundance ratios are expressed in terms of the Solar value: $Z_{\rm C,\odot} = 0.00218$ (mass fraction of carbon in the Sun; Asplund, Grevesse & Sauval 2005).

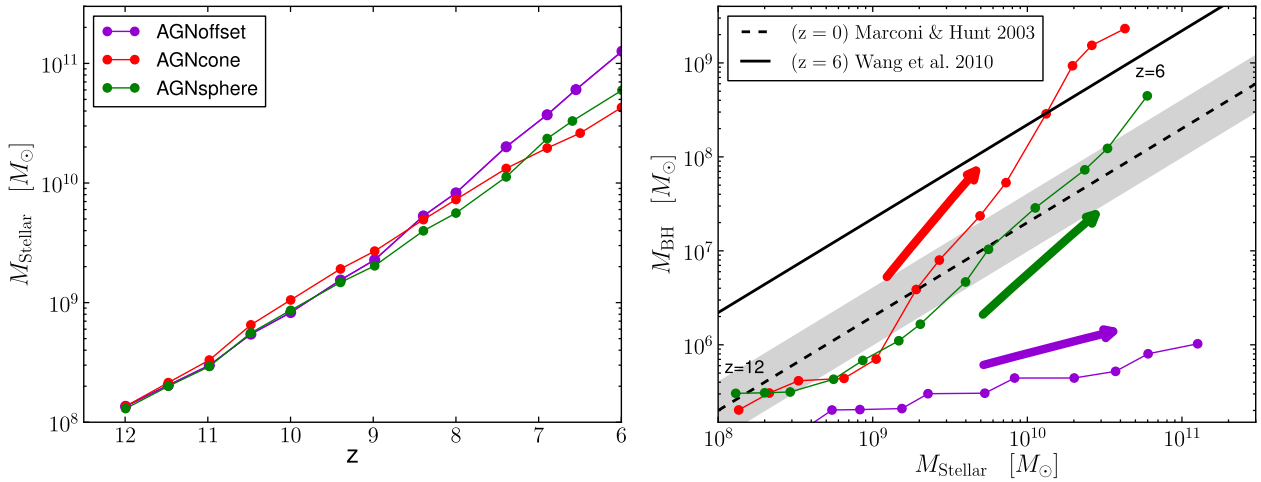

Figure 4. Left-hand panel: Redshift evolution of the stellar mass of the host galaxy of the most-massive BH progenitor. The plotting colour denote different runs: *AGNoffset* – violet, *AGNcone* – red, *AGNsphere* – green. Right-hand panel: Redshift track of the BH mass versus host galaxy stellar mass of the most-massive BH progenitor (which was plotted in Fig. 2). The thick arrows denote the direction of time evolution (going from high to low z) for the three runs. The starting ($z = 12$) and ending ($z = 6$) redshifts are written near the relevant points on the tracks. The black lines indicate the observed BH mass versus stellar bulge mass relation of: local galaxies (Marconi & Hunt 2003) as the dashed line, and $z \sim 6$ quasars (Wang et al. 2010) as the solid line.

In the *noAGN* run (left column), weak outflows ($v_{\rm r} < 300\,{\rm km\,s^{-1}}$) develop bounded within $0.5R_{200}$ as warm-hot ($T \sim 10^6$ K) halo gas. It is caused by SN feedback and galaxy merger shocks. The $Z_{\rm C}$ distribution is more centrally concentrated in this case. Such a high-mass ($M_\star \sim 10^{11}\,{\rm M}_\odot$) galaxy cannot efficiently drive outflows with only SN feedback (e.g. Benson et al. 2003; Talia et al. 2017).

The other two simulations (*AGNcone* and *AGNsphere*) show the formation of BH feedback-induced outflows, which are hot ($T \sim 10^8$ K) – visible as yellow and red areas in the temperature plot, and consist of low-density, metal-enriched gas. The outflows are fastest ($v_{\rm r} > 2000\,{\rm km\,s^{-1}}$) in run *AGNcone* (right column, where the BHs become more-massive than the other runs), extended bipolar shaped, propagating to beyond the galaxy R_{200} (black dashed circle). The outflows reach $v_{\rm r} \sim 1500\,{\rm km\,s^{-1}}$ in run *AGNsphere* (middle column), are more spherical shaped and limited within R_{200}. They disrupt the cold dense filamentary gas inflows to the galaxy centre, along the direction of outflow propagation. This quenches star formation, and halts the formation of nearby satellite galaxies. It is revealed by the disrupted clumps and lack of star-forming dense filaments near the central galaxy in runs *AGNcone* and *AGNsphere*, as compared to run *noAGN* (which we quantify later in Section 3.7). The outflows transport metals away from star-forming regions, and enrich the surrounding circumgalactic medium out to R_{200}. Some inflows of cold, dense gas continue to occur perpendicular to the outflow direction.

We find that the density increment, at the edges of the outflow shocks, remains below the SF threshold density $n_{\rm SF}$. Therefore, no new star formation is triggered in our simulations by AGN feedback. This might be a numerical resolution effect, since our resolution (length scale of 1 kpc comoving) is lower than those where positive feedback from AGN is simulated in galaxies (e.g. Bieri et al. 2015).

3.5.2 *Gas radial velocity*

The radial velocity ($v_{\rm r}$) histogram of gas at $z = 6$ is plotted in Fig. 6. The three panels display gas within distinct regions: at $r = R_{200} \pm 2$ kpc comoving (left), inside $r \leq R_{200}$ (middle) and all the gas within simulation volume (right). Each curve shows the mass fraction of gas per velocity bin, and the histogram is normalized to the total gas mass within the plotted region. The coloured dashed lines in the right-hand panel indicate the halo escape velocity in each run, $v_{\rm esc} = \sqrt{2\,G\,M_{\rm halo}/R_{200}}$ (for galaxy total halo mass $M_{\rm halo}$).

The $v_{\rm r}$ distribution in the run *AGNoffset* (violet curve) is almost coincident with that in *noAGN* (blue), because there the BHs do not exert enough feedback. The velocities are the lowest in these two cases, reaching a maximum $v_{\rm r} \sim 800\,{\rm km\,s^{-1}}$ within the virial radius.

We find a larger fraction of outflowing ($v_{\rm r} > 0$) and a smaller fraction of inflowing ($v_{\rm r} < 0$) gas in runs *AGNcone* (red) and *AGNsphere* (green), when compared to *noAGN*; which we quantify in Section 3.5.3. Powerful high-velocity outflows are created by AGN feedback in these two runs, where the BHs grow supermassive. Gas reaches a maximum $v_{\rm r} \sim 1400\,{\rm km\,s^{-1}}$ in *AGNsphere* and $v_{\rm r} > 2000\,{\rm km\,s^{-1}}$ in *AGNcone*. Our simulation velocity values are consistent with the observations of $z > 6$ quasar outflows by Maiolino et al. (2012) and Cicone et al. (2015), where the gas traced by [C II] is moving at high velocities, up to $\sim$1400 km s^{-1}. However, note that the bulk of our simulated outflows consist of shock-heated gas of $T > 10^6$ K. While [C II] observations probe cold gas of a few 100 s K.

Our $v_{\rm r}$ values (1400–2000 km s^{-1}) also agree well with previous zoom-in simulation studies of quasar outflows. Costa et al. (2014) found that AGN-driven outflows are highly anisotropic, pushing gas at $\geq$1000 km s^{-1} out to tens of kpc. Costa, Sijacki & Haehnelt (2015) deduced that parts of hot AGN outflows, propagating through a clumpy medium pre-enriched with metals from SN, can cool radiatively, resulting in velocity widths of cold gas up to $\sim$2000 km s^{-1}.

3.5.3 *Outflow and inflow fractions of gas*

The radial[2] distribution of inflow and relevant outflow gas fractions is plotted in Fig. 7. The inflowing ($v_{\rm r} < 0$) mass fraction is in the

[2] The radius is computed as the distance from the gravitational potential minimum of the galaxy, which is an output of the *SubFind* subhalo finder.

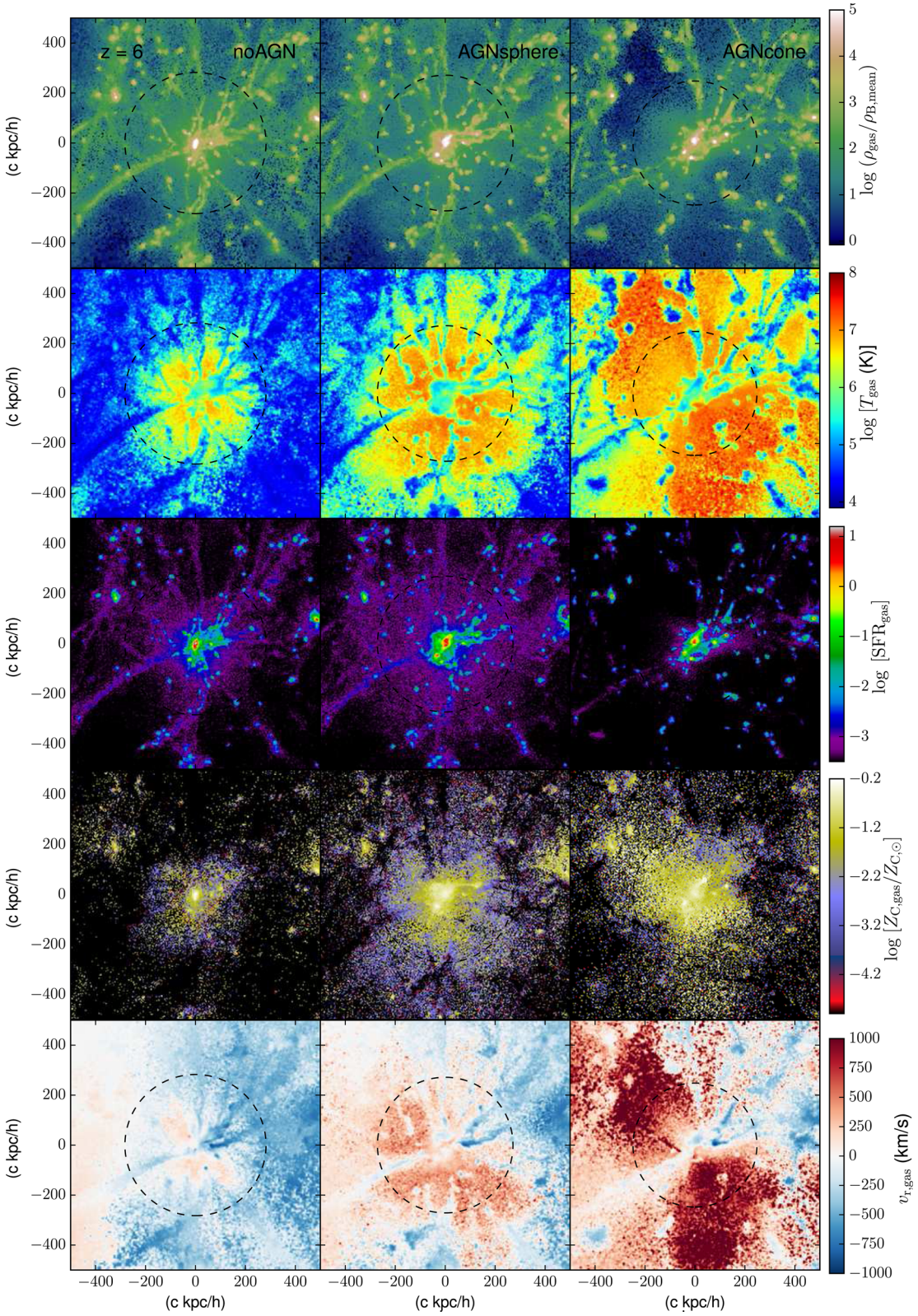

Figure 5. Projected gas kinematics in a $(500\,h^{-1}\,\mathrm{kpc})^3$ comoving volume around the most-massive galaxy at $z = 6$. The five rows indicate gas properties: overdensity (first row – top), temperature (second), SFR (third), carbon abundance (fourth) and radial velocity (fifth – bottom). The three columns are different simulations: *noAGN* (left), *AGNsphere* (middle) and *AGNcone* (right). The black dashed circle depicts the galaxy virial radius R_{200} in each case.

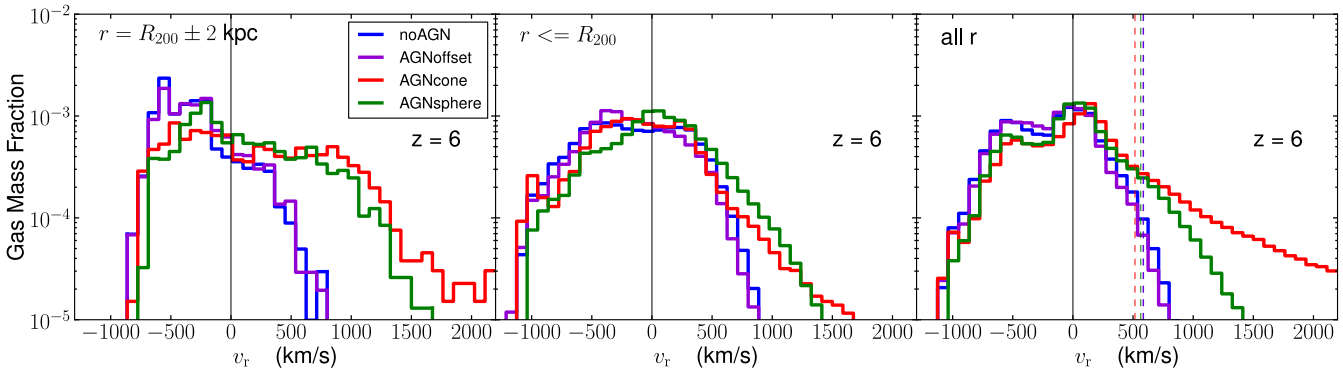

Figure 6. Radial velocity histogram of gas within given regions around the most-massive galaxy at $z = 6$, in four simulations: *noAGN* – blue curve, *AGNoffset* – violet, *AGNcone* – red, *AGNsphere* – green. The regions are gas at $r = R_{200} \pm 2$ kpc (left-hand panel), gas inside $r \leq R_{200}$ (middle) and all the gas within simulation volume (right). Each curve shows the mass fraction of gas per velocity bin, and the histogram is normalized to the total gas mass within the plotted region. The vertical black solid line is $v_r = 0$. The coloured dashed lines in the right-hand panel indicate the halo escape velocity in the four runs.

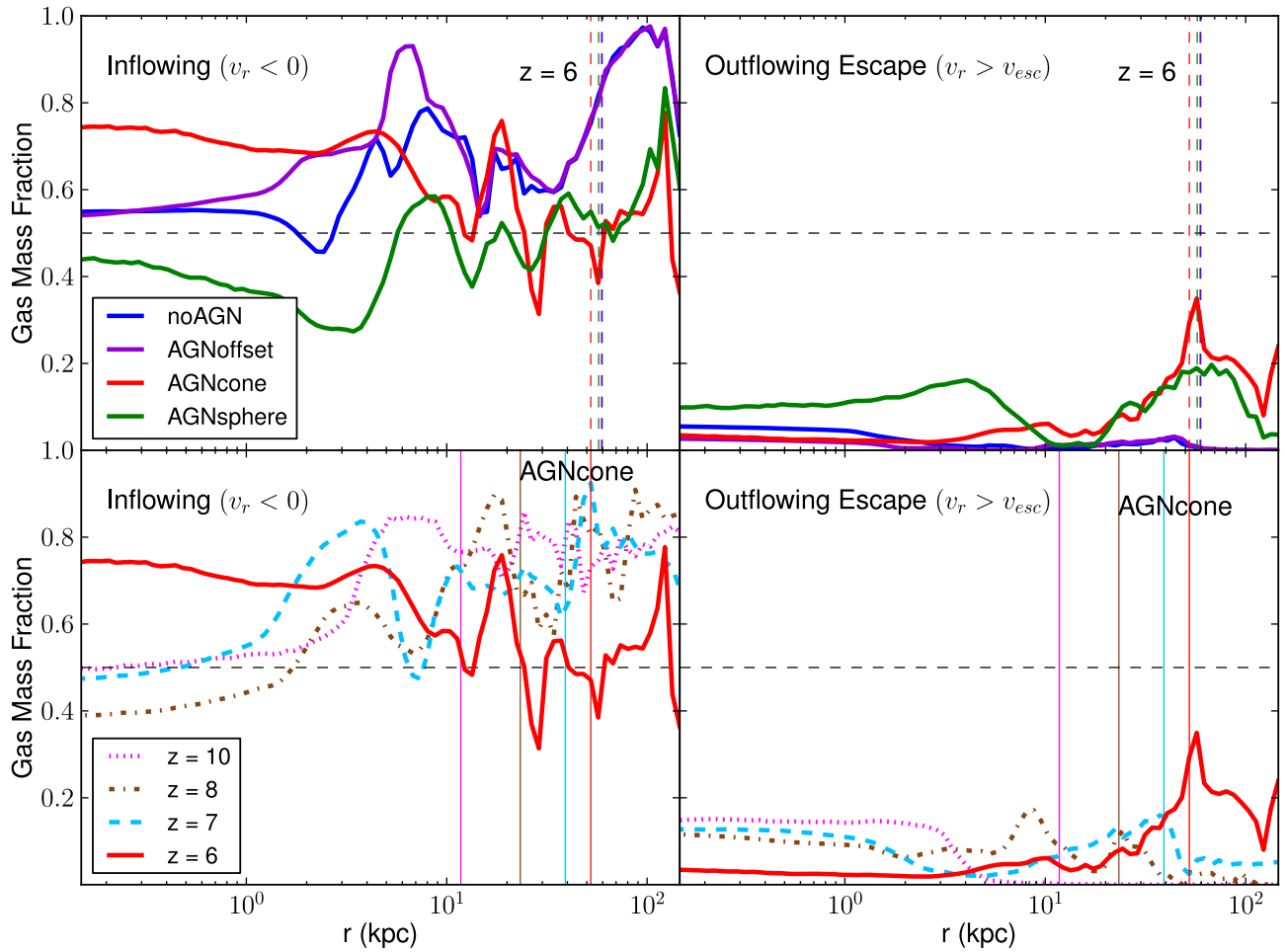

Figure 7. Gas mass fraction inflowing ($v_r < 0$) in the left column, and outflowing at above the escape velocity ($v_r > v_{esc}$) at the right column, versus radius of the most-massive galaxy in the simulations. Top row displays results at $z = 6$ of four runs: *noAGN* – blue, *AGNoffset* – violet, *AGNcone* – red, *AGNsphere* – green. Bottom row is at four redshifts of a single run *AGNcone*: $z = 10$ – magenta dotted, $z = 8$ – brown dot–dashed, $z = 7$ – deepskyblue dashed and $z = 6$ – red solid. Each curve shows the in/out-flowing mass as a fraction of gas contained in the radial bins. The vertical coloured lines (dashed in the top panels and solid in the bottom) indicate the halo virial radius R_{200} in a respective run at the relevant redshift. Note that the radial coordinate (x-axis) is in units of physical kpc.

left column, which quantifies the inflow of cosmic gas and satellite galaxies. Gas fraction whose radial velocity is positive and exceeds $v_{\rm esc}$ ($v_{\rm r} > v_{\rm esc}$) is at the right column, which indicates outflowing gas that can escape the halo potential.

The top row of Fig. 7 presents the results of four runs at $z = 6$. Near and beyond the virial radius R_{200}, the inflow mass fraction in the run *AGNoffset* (violet curve) is same as that in *noAGN* (blue), because there the BHs are too small. Whereas BH feedback induced outflows are created in the runs *AGNcone* (red) and *AGNsphere* (green): the inflow fraction around R_{200} is lower by 30 per cent than in the *noAGN* run, and consequently the outflowing escape fraction is higher by 30 per cent. The peaks in the inflow fraction curve correspond to accreting satellite galaxies and clumps, which occurs at different radii for each run. As an example, the inflow fraction in the inner regions at $r < 5$ kpc is the highest in run *AGNcone* ($\sim$70 per cent) compared to all other cases. This is because the AGN feedback process changes the merger history in the inner parts of the galaxy. The time taken by inner satellites to merge is larger in the presence of AGN feedback (also visible as the density substructures in the top panels of Fig. 5), because of disruption by powerful outflows.

The bottom row of Fig. 7 denotes the fractions at four redshifts in the run *AGNcone*, which visualizes the time evolution of the impact of AGN feedback. The inflow fractions near R_{200} remain almost similar from $z = 10$ to $z = 7$. Feedback from the BH has a visible impact at $z = 6$, when the inflow fraction reduces by 30 per cent at the galaxy outskirts ($r \sim$ 20–200 kpc), and a similar fraction escapes the halo while outflowing.

We find that BH outflows suppress cosmic gas inflows by 30 per cent near R_{200} at $z = 6$, and causes (20–30) per cent of the gas to reach velocities in excess of the halo escape speed. It also alters the merger history and substructure distribution in the inner parts of the galaxy.

3.5.4 *Mass outflow rate*

We measure outflowing gas using spherical shell volumes around galaxies. Gas particles (the ith particle having a mass m_i) lying inside a shell, at radius r of thickness Δr, are selected. We calculate the mass outflow rate by summing over the particles inside Δr having a radial velocity larger than the escape speed ($v_{\rm r} > v_{\rm esc}$):

$$\dot{M}_{\rm out}(r) = \sum_{v_{{\rm r},i} > v_{\rm esc}} \frac{m_i |v_{{\rm r},i}|}{\Delta r}. \quad (12)$$

We plot in Fig. 8 the gas mass (top row), outflow velocity (middle row) and $\dot{M}_{\rm out}$ (bottom row) versus radius, at four redshifts (in the four columns). Note that the radial coordinate (x-axis) is in units of physical kpc in this figure. The profiles are the same for all the four runs at $z = 10$ (left column), when the BHs are too small ($M_{\rm BH} < \sim 10^6\,{\rm M}_\odot$) to produce a dynamically relevant influence. AGN feedback effects start to be seen at $z = 8.6$ (second column) in the run *AGNsphere* (green curve), which also suppressed star formation from similar epochs (see Fig. 2 bottom-left panel).

The total gas mass is computed as $M_{\rm gas} = \sum_{\rm all-}{}_{v_{r,i}} m_i$. At $z \geq 8.6$ (three right columns), $M_{\rm gas}$ inside 2 physical kpc is up to 10 times lower in runs *AGNcone* and *AGNsphere*, compared to the *noAGN* case. This is because AGN feedback ejects central gas and reduces the inner gas content.

The next two rows of Fig. 8 show properties of only the gas outflowing at above the escape velocity ($v_{\rm r} > v_{\rm esc}$). The outflow radial velocity is in the middle row, where the solid curves depict the median-$v_{\rm r}$. The radial scatter of the $v_{\rm r}$ distribution is displayed for two runs as the shaded areas, showing the 95th percentiles above and below the median-value. The ejection of outflows from the centre are visible as the rise in the scatter of run *AGNcone* (pink shaded area), with some gas reaching $v_{\rm r} > 2000\,{\rm km\,s^{-1}}$ at $z = 7.4$ and 6.4. Whereas in the *noAGN* run, the scatter (grey shaded area) is always small, limited to $v_{\rm r} \leq 800\,{\rm km\,s^{-1}}$. The mass outflow rate is in the bottom row. In the outer regions $r \geq 1$ kpc, the $\dot{M}_{\rm out}$ is higher in the strong AGN feedback runs (*AGNcone* and *AGNsphere*) at $z \geq 8.6$ (three right columns).

Observational data of outflow velocity and mass-loss rate versus distance (figs 5 and 8 of Cicone et al. 2015) at $z = 6.4$ are overplotted in the middle-right and bottom-right panels as the black asterisk symbols. The $v_{\rm out} \sim 1000\,{\rm km\,s^{-1}}$ observed points agree well with the median-$v_{\rm r}$ from our simulation *AGNcone*. Such extended ($r >$ 8–10 kpc) high-velocity outflows cannot be explained with SF and SN-driven feedback only (e.g. Valiante et al. 2012).

In the observed radii range, $r =$ 3–30 kpc, the $\dot{M}_{\rm out}$ in our strong AGN feedback runs is 10–100 times higher than the *noAGN* case. The observational $\dot{M}_{\rm out}$ between $r = 3$ and 15 kpc agree well with our results in the *AGNcone* run. However, in the outer regions $r =$ 15–60 kpc our simulations predict an almost flat $\dot{M}_{\rm out}$ versus r, while the observations show a steep decline of $\dot{M}_{\rm out}$ with r. This discrepancy is partly because of the different method used to measure the outflow rate in Cicone et al. (2015). The radial distance of the outflowing clouds from the galaxy centre is used in the denominator of equation (12), i.e. $\dot{M}_{\rm out}(r) = \sum \frac{m_i |v_{{\rm r},i}|}{r_i}$. There is also the contribution of observational uncertainties. The decreasing $\dot{M}_{\rm out}$ with radius at $r \geq$ (20–30) kpc may be in part due to instrument sensitivity issues, and/or the outflowing clouds being ablated by dynamical instabilities or photoevaporated (for a discussion see Ferrara & Scannapieco 2016). We finally note that for a fair comparison, the simulations must be processed to extract mock spectra; and $\dot{M}_{\rm out}$ computed henceforth using r exactly like the way done in observational analyses.

The observed integrated outflow rate obtained by adding up the mass-loss rate contributions from all the outflowing clumps is $1400 \pm 300\,{\rm M}_\odot\ {\rm yr}^{-1}$ (Cicone et al. 2015). Using the same nine bins as the observations, we obtain an integrated mass outflow rate of $128\,{\rm M}_\odot\ {\rm yr}^{-1}$ in run *noAGN*, and $2067\,{\rm M}_\odot\ {\rm yr}^{-1}$ in run *AGNcone*. Thus, we conclude that the high outflow rate detected in observations are driven by the central quasar; and not by star formation activities.

3.6 Radial profiles of gas properties

We plot in Fig. 9 the radial profiles of gas overdensity (left-hand panel), temperature (middle) and SFR surface density (right-hand panel). Note that in the T profiles, the gas with $\rho > n_{\rm SF}$ have been marked with the yellow shaded region, because the temperature of such dense gas is not predicted correctly, but set to the effective equation state describing the SF model (for details see fig. 1 of Springel & Hernquist 2003).

The top row displays the results of four runs at $z = 6$. The density and SFR profiles have similar trends, which is expected because star formation in the gas is solely dependent on density (our model Section 2.2). At larger radii ($r >$ 10 kpc), the median density and SFR of all the runs are almost indistinguishable from each other. The radial profiles in the run *AGNoffset* (violet curve) is similar to that in *noAGN* (blue) at all radii, because here the BHs do not grow massive enough and there is no efficient feedback.

In the *AGNcone* (red curve) and *AGNsphere* (green) runs, where the BHs become supermassive, the density and SFR are

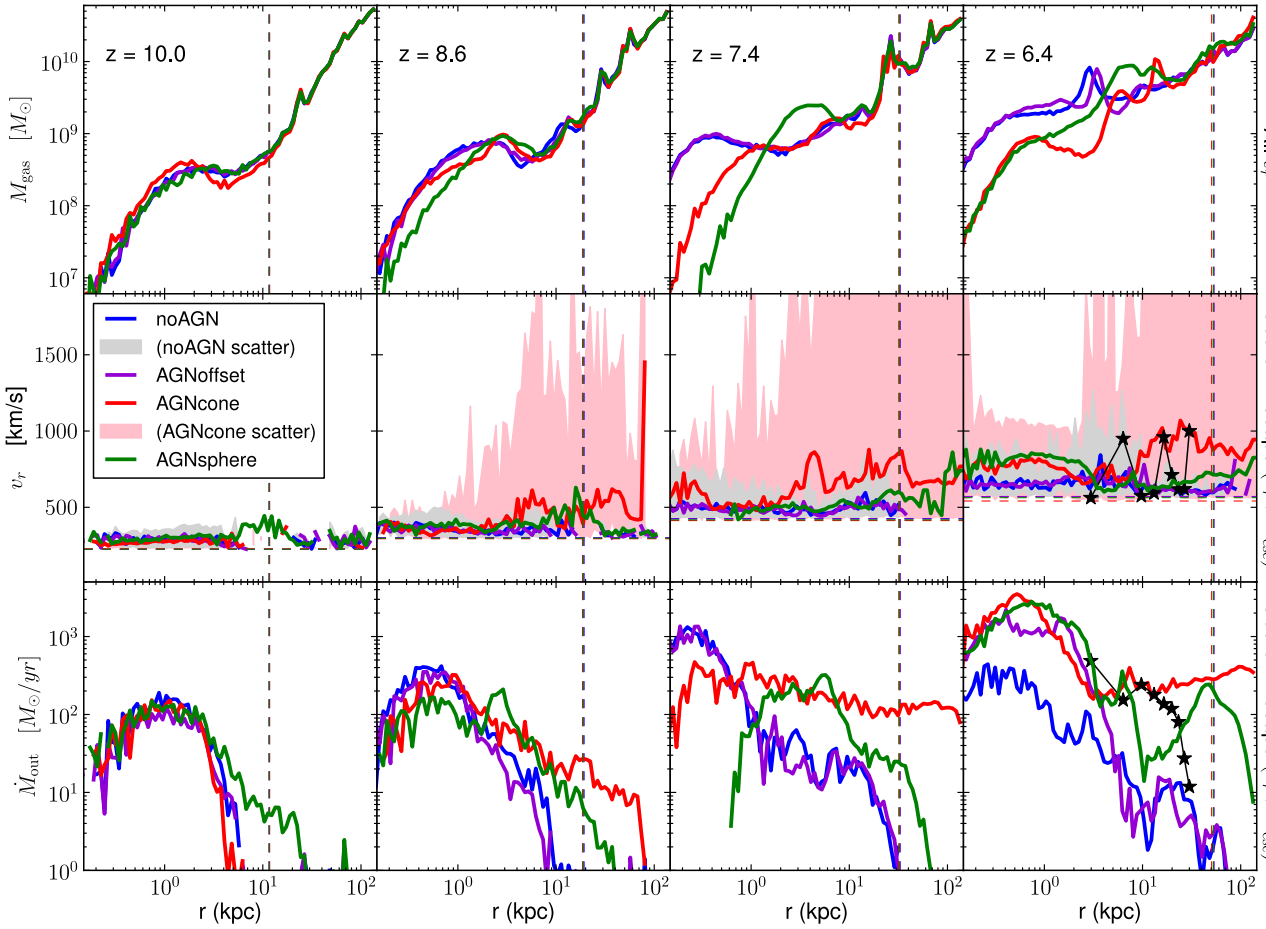

Figure 8. Radial distributions of gas around the most-massive galaxy in the simulations: top row shows the total (any v_r) gas mass. The next two rows show properties of only the gas outflowing at above the escape velocity ($v_r > v_{esc}$): median outflow radial velocity in the middle row, and mass outflow rate in the bottom row. Four redshifts are plotted in the columns from left: $z = 10$, 8.6, 7.4, 6.4. In each panel, the colours distinguish four runs: *noAGN* – blue, *AGNoffset* – violet, *AGNcone* – red, *AGNsphere* – green; with the vertical coloured dashed lines indicating the halo virial radius (R_{200}). The radial scatter of the v_r distribution is displayed in the middle row for two runs: *noAGN* – grey shaded area, *AGNcone* – pink shaded area; showing the 95th percentiles above and below the median-v_r. Observational data of outflow velocity and mass-loss rate versus distance (Cicone et al. 2015) at $z = 6.4$ are overplotted in the middle-right and bottom-right panels as the black star symbols. Note that the radial coordinate (x-axis) is in units of physical kpc.

10–100 times lower at $r \leq 10$ kpc than in the *noAGN* run. This is due to the central BH, which accretes some gas in and ejects out feedback energy. Some central gas is expelled in the form of high-velocity outflows, which thermalize their kinetic energy and shock-heat the galaxy outskirt regions. This heating is exhibited by the median temperature (top-middle panel) remaining high $T \sim 5 \times 10^6$ K, in the outer regions at $r \sim 20$–100 kpc.

The bottom row of Fig. 9 presents the profiles at four redshifts in the run *AGNcone*. It visualizes the time evolution of the impact of AGN feedback on gas radial properties. Initially, the density and consequently SFR profiles increase at all radii from $z = 10$ (magenta dotted curve) to $z = 8$ (brown dot–dashed), and somewhat further to $z = 7$ (deepskyblue dashed). During galaxy formation, gas inflows and collapses to form dense structures where stars form. Feedback from the BH acts between $z = 7$ and $z = 6$ (red solid curve), when the central (at $r < 5$–6 kpc) density drops by a factor 30 and the central SFR reduces by a factor 10. The temperature at the galaxy outskirts ($r \sim 70$–700 kpc) is $T \sim 10^4$ K at $z = 10$. It increases steadily, by heating from dynamical merger shocks as well as AGN feedback-induced outflows, to reach $T \sim 5 \times 10^6$ K at $z = 6$.

Observational data of SFR surface density in the host galaxy of the quasar SDSS J1148 at $z = 6.4$ is overplotted in the right-hand panels. Our simulations reproduce the SFR surface density of the extended component (Cicone et al. 2015) between $r = 1$–10 kpc. However, the results in the *AGNcone* run remains below the compact component (Walter et al. 2009) by a factor $\geq$10, while the runs *noAGN* and *AGNoffset* are above it by a factor $\sim$2. These imply that the observed quasar SDSS J1148 represents a stage in its evolution when star formation is not quenched significantly at the centre.

We summarize that BH feedback decreases gas density at the galaxy centre by a factor 100, and increases gas temperature near R_{200} by a factor 50. The former leads to a reduction of SFR surface density by up to a factor 1000 within 10 kpc from the galaxy centre. Powerful BH outflows are launched at epochs between $z = 7$ and $z = 6$, which heats up the circumgalactic and intergalactic medium.

3.7 Star formation quenching mechanism

The fraction of outflowing, inflowing and dense gas as a function of BH mass at $z = 6$ is plotted in Fig. 10. The mass fraction in each simulation is computed with respect to all the gas within the zoomed-in region. The left-hand panel shows outflowing gas fraction computed using two conditions: gas with radial velocity larger

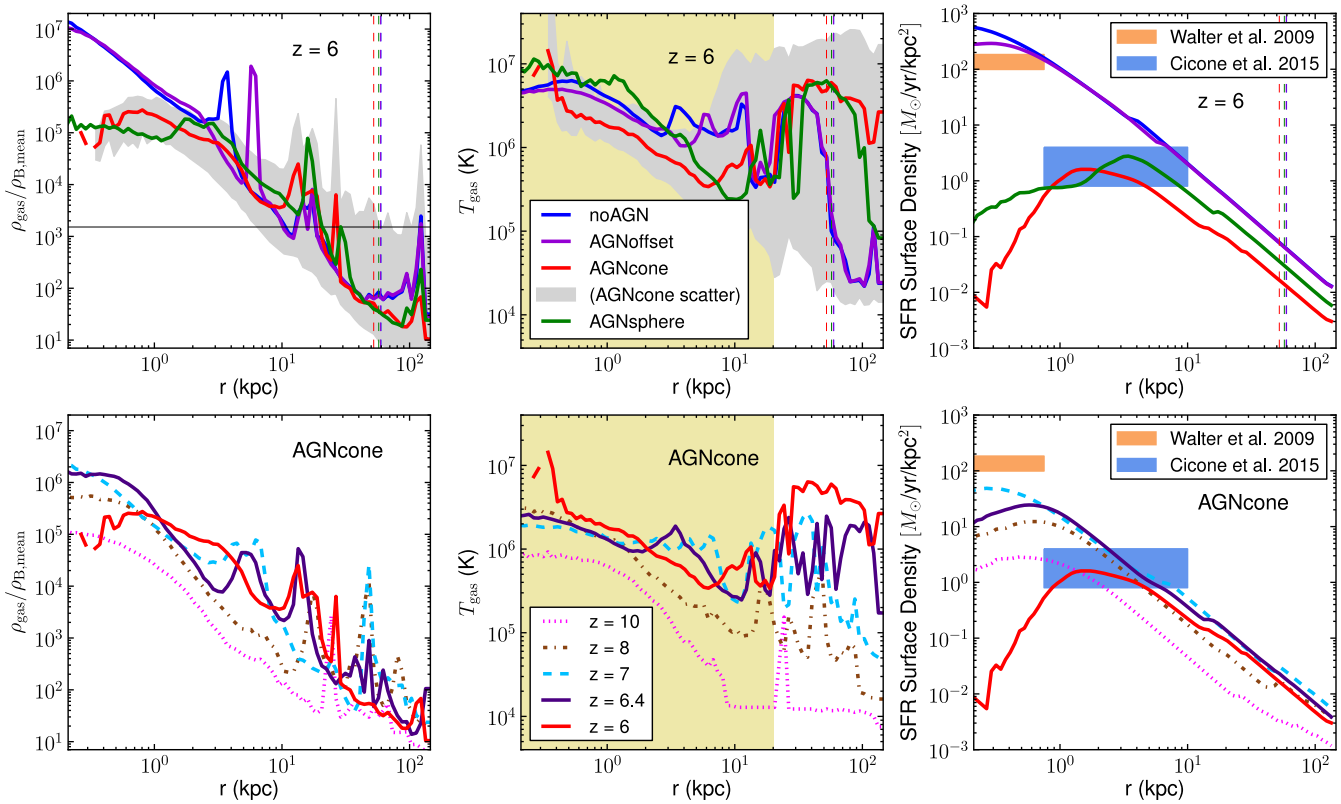

Figure 9. Radial profiles of gas properties around the most-massive galaxy: overdensity in the left column, temperature at the middle column and SFR surface density in the right column. Note that the radial coordinate (x-axis) is in units of physical kpc. The plotted ρ and T curves denote the median quantity in radial bins of each run. The grey shaded area enclose the 90th percentiles above and below the median of run *AGNcone*, as a representative of the radial scatter. Top row presents the results at $z = 6$, with the colours distinguishing four simulations: *noAGN* – blue, *AGNoffset* – violet, *AGNcone* – red, *AGNsphere* – green. The vertical coloured dashed lines in the top panels indicate the halo virial radius (R_{200}) in the runs. The horizontal black line in the top-left panel denotes the star formation threshold density ($n_{\rm SF}$, Section 2.2). In the T profiles, the gas with a density higher than $n_{\rm SF}$ have been marked with the yellow shaded region; since the temperature of such dense gas is not predicted correctly within our SF model. Bottom row displays the profiles in a single run *AGNcone* at four redshifts: $z = 10$ – magenta dotted, $z = 8$ – brown dot–dashed, $z = 7$ – deepskyblue dashed and $z = 6$ – red solid. Observational data is overplotted in the SFR surface density profiles: a compact component (Walter et al. 2009) as the orange shade, and an extended component (Cicone et al. 2015) as the blue shaded area.

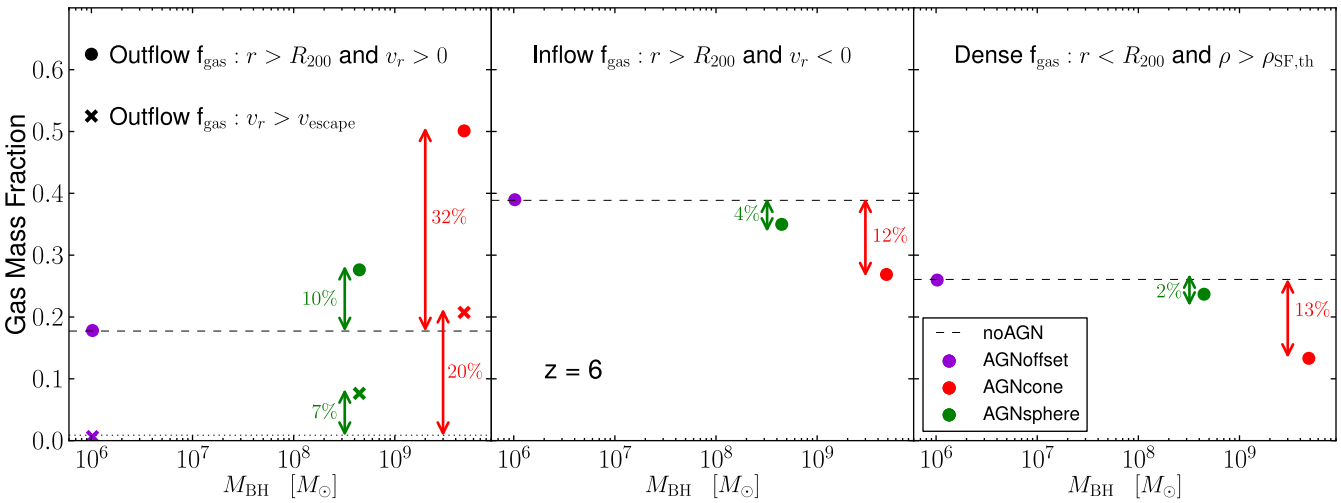

Figure 10. Mass fraction of outflowing, inflowing and dense gas as a function of BH mass, at $z = 6$. Left-hand panel shows outflowing gas fraction computed in two ways: gas with radial velocity larger than the halo escape velocity ($v_{\rm r} > v_{\rm escape}$) as the cross symbols, and outgoing gas outside the halo virial radius ($r > R_{200}$ and $v_{\rm r} > 0$) as the filled circles. Middle panel shows inflowing gas fraction outside the virial radius ($r > R_{200}$ and $v_{\rm r} < 0$). Right-hand panel shows gas fraction denser than the star formation threshold density inside the virial radius ($r < R_{200}$ and $\rho > \rho_{\rm SF,th}$). Each of the three points is for one AGN simulation, as distinguished by the colour. The horizontal black-dashed line (and the black-dotted line in the left-hand panel) indicates the corresponding fraction in the *noAGN* run. The fraction in each simulation is computed with respect to all the gas within the zoomed-in volume.

than the halo escape velocity ($v_r > v_{escape}$) as the cross symbols, and outgoing gas outside the halo virial radius ($r > R_{200}$ and $v_r > 0$) as the filled circles. The middle panel shows inflowing gas fraction outside the virial radius ($r > R_{200}$ and $v_r < 0$). The right-hand panel shows gas fraction denser than the star formation threshold density inside the virial radius ($r < R_{200}$ and $\rho > \rho_{SF,\,th}$).

Similar to the other results in run *AGNoffset* (violet point), where the BHs do not grow, the gas fractions are the same as that in the *noAGN* case (horizontal black-dashed line in all panels, and the black-dotted line in the left-hand panel). Effects of BH feedback and the subsequent outflows created can be seen in runs *AGNcone* (red) and *AGNsphere* (green) as the higher outflowing fractions, lower inflowing fraction and lower dense fraction. We find a positive correlation of the outflowing gas mass fraction with the central BH mass in galaxies.

The differences caused by the most-massive BH, compared to the SF-only case, is written as the percentage value in each panel. A central BH of $M_{BH} = 4 \times 10^9\,M_\odot$ unbinds 20 per cent of the gas in and around its host galaxy, which outflows with $v_r > v_{escape}$ and escapes the halo. It makes 32 per cent more gas outside R_{200} to outflow. It reduces the inflow fraction outside R_{200} by 12 per cent. It lowers the high-density (denser than $\rho_{SF,\,th}$) gas fraction inside R_{200} by 13 per cent. All these processes limit the gas available for star formation.

Our results are consistent with recent hydrodynamical simulation analyses by Beckmann et al. (2017), who concluded that SMBHs affect their host galaxies through a combination of outflows and disruption of central gas inflows, which acting together drops net inflows by up to 70 per cent.

We deduce that AGN feedback effects quench star formation in galaxies by a combination of mechanisms. The cosmic inflow fraction lowered is comparable to the dense gas fraction reduced. Fast outflowing gas ejected away affects twice the fraction of gas as compared to the two above, which is hence the dominant process.

4 SUMMARY AND CONCLUSIONS

Quasars are observed with SMBHs at their centres, some hosting powerful outflows, even at high redshifts. We investigate the impact of AGN feedback in massive galaxies in the early Universe, and probe $z \geq 6$ quasar outflows, using numerical simulations. We employ a modified version of the SPH code GADGET-3. It includes the following subresolution physics: radiative cooling and heating from photoionizing background, star formation, stellar evolution, chemical enrichment for 11 elements, supernova feedback, AGN accretion and feedback. We use novel methods to distribute the feedback energy from a BH in the kinetic form, where the velocity of the neighbouring gas is incremented.

We perform zoomed-in cosmological hydrodynamical simulations of quasar-host galaxies. A $(500\,Mpc)^3$ comoving volume is first evolved from $z = 100$ using 256^3 DM particles. We select the most-massive halo at $z = 6$ of total mass $4.4 \times 10^{12}\,M_\odot$, and zoom-in a cubic region of side $2R_{200} \simeq 1022$ kpc comoving. The Lagrangian volume of $(5.21\,Mpc)^3$, tracked back to our initial condition at $z = 100$, is populated with high-resolution DM and baryon particles. The gas particle mass is $1.41 \times 10^6\,M_\odot$, and the gravitational softening length is $1\,h^{-1}\,kpc^{-1}$ comoving. The zoom-in simulation is finally evolved from $z = 100$ up to $z = 6$, containing high-resolution particles in the $(5.21\,Mpc)^3$ volume, embedded inside the $(500\,Mpc)^3$ low-resolution periodic box.

We execute four runs: one of them is a control simulation with SF-only and no BH; the other three runs are with AGN feedback exploring different subresolution models for the BHs. In our simulation input model, we seed BHs of mass $10^5\,M_\odot$ at the centres of massive haloes with $M_{halo} > 10^9\,M_\odot$. The earliest BHs appear at $z \sim 15$. The BHs are allowed to grow by accreting surrounding gas and by merger with other BHs. As they accrete and grow, the BHs eject out feedback energy. We analyse the simulations by exploring the growth of the first SMBHs, their coevolution with galaxies and the generated outflows. We find the following results from our simulations:

(i) The BHs grow to supermassive ($M_{BH} \sim 10^9\,M_\odot$) only when we implement the repositioning or advection model, where a BH is repositioned to the centre of its host galaxy. The BHs then accrete gas at the Eddington accretion rate over $z = 9$–6, by encountering galaxy-central high-density gas. The most-massive BH at $z = 6$ has: $M_{BH} = 4 \times 10^9\,M_\odot$ and $\dot{M}_{BH} = 100\,M_\odot\,yr^{-1}$.

(ii) Massive BHs at galaxy centres mostly occur as merging systems at $z = 6$–7, and leads to the formation of an SMBH binary or triplet. This prediction makes a strong case to observe them at high-z in the future.

(iii) The BHs are too small ($M_{BH} \sim 10^6\,M_\odot$) in the case without BH repositioning. The growth is dominated by mergers, since gas density and consequently accretion rate is always low. The results here are similar to that in the noAGN case, because there is no effective AGN feedback.

We see the following AGN feedback impacts when the BHs grow supermassive $M_{BH} \geq 10^8$–$10^9\,M_\odot$.

(i) Star formation is quenched between $z = 8$ and 6, when the BHs have reached $M_{BH} > 10^7\,M_\odot$. The total SFR is reduced by a factor 5 (to $200\,M_\odot\ yr^{-1}$), and the SFR surface density lowered by 1000 near the galaxy centre.

(ii) The SMBHs in massive galaxies ($M_\star > 10^9\,M_\odot$) at $z = 8$–6 are more-massive than expected from the local [M_{BH}–$M_\star$] correlation; and the same scenario is indicated by observations at $z \geq 6$.

(iii) Bipolar bubble-like high-velocity ($v_r \sim 1400$–$2000\,km\,s^{-1}$) outflows form at epochs $z = 7$ to $z = 6$, originating from the BH. The outflows are hot, consist of shock-heated low-density gas, and propagate beyond the galaxy virial radius, R_{200} (i.e. up to a few hundreds kpc).

(iv) Cold dense filamentary cosmic gas inflows are disrupted by the AGN outflow-driven forward shocks, and reduced by a factor 30 per cent near $r = R_{200}$ (and by 12 per cent considering the gas outside R_{200}) at $z = 6$. This halts the formation of satellites, thus altering the substructure distribution in the inner parts of the galaxy. While at the same time, significant amounts of gas (∼30–40 per cent) continue to inflow towards the central region, perpendicular to the outflow direction.

(v) The density of gas is decreased at the galaxy centre ($r < 10$ kpc) by a factor 100. The temperature is increased at the outskirts ($r \sim 100$–800 kpc) by a factor 50.

(vi) A fraction ∼20 per cent of the total gas outflows with a velocity larger than the escape speed, thus being able to escape the galaxy. While in the noAGN case, no gas can escape from the galaxy. There is a positive correlation between the outflowing gas fraction and the central BH mass.

We deduce that AGN feedback quenches star formation in galaxies by a combination of mechanisms: ejecting gas out of the galaxy halo at high velocity, reducing the amount of dense gas, as well as halting gas inflows.A BH of $M_{BH} = 4 \times 10^9\,M_\odot$ drives 32 per cent more gas outside R_{200} as outflows (with 20 per cent larger

fraction above the $v_{\rm escape}$), reduces the inflow fraction outside R_{200} by 12 per cent, and lowers the high-density (denser than $\rho_{\rm SF,\,th}$) gas fraction inside R_{200} by 13 per cent. All these processes limit the gas available for star formation. The dominant contribution to this effect comes from fast, powerful outflows ejecting gas out of the host galaxy halo.

ACKNOWLEDGEMENTS

We thank the referee for useful comments which helped to clarify the paper. We are most grateful to Volker Springel for allowing us to use the GADGET-3 code. We thank Giuseppe Murante, Klaus Dolag and Alexander Beck for technical help with the code. This work is supported by the PRIN-INAF 2014 grant 'Windy black holes combing galaxy evolution'. CC acknowledges funding from the European Union's Horizon 2020 research and innovation programme under the Marie Sklodowska-Curie grant agreement No. 664931. RM acknowledges support from the Science and Technology Facilities Council (STFC) and from the ERC Advanced Grant 695671 'QUENCH'. SC acknowledges financial support from the STFC.

REFERENCES

Andrade-Santos F., Bogdan A., Romani R. W., Forman W. R., Jones C., Murray S. S., Taylor G. B., Zavala R. T., 2016, ApJ, 826, 91
Asplund M., Grevesse N., Sauval A. J., 2005, in Barnes T. G. III, Bash F. N., eds, ASP Conf. Ser. Vol. 336, Cosmic Abundances as Records of Stellar Evolution and Nucleosynthesis in honor of David L. Lambert. Astron. Soc. Pac., San Francisco, p. 25
Barai P., 2008, ApJ, 682, L17
Barai P., Martel H., Germain J., 2011, ApJ, 727, 54
Barai P. et al., 2013, MNRAS, 430, 3213
Barai P., Viel M., Murante G., Gaspari M., Borgani S., 2014, MNRAS, 437, 1456
Barai P., Monaco P., Murante G., Ragagnin A., Viel M., 2015, MNRAS, 447, 266
Barai P., Murante G., Borgani S., Gaspari M., Granato G. L., Monaco P., Ragone-Figueroa C., 2016, MNRAS, 461, 1548
Beck A. M. et al., 2016, MNRAS, 455, 2110
Beckmann R. S. et al., 2017, MNRAS, 472, 949
Benson A. J., Bower R. G., Frenk C. S., Lacey C. G., Baugh C. M., Cole S., 2003, ApJ, 599, 38
Bieri R., Dubois Y., Silk J., Mamon G. A., 2015, ApJ, 812, L36
Bieri R., Dubois Y., Rosdahl J., Wagner A. Y., Silk J., Mamon G. A., 2017, MNRAS, 464, 1854
Biffi V. et al., 2016, ApJ, 827, 112
Bondi H., 1952, MNRAS, 112, 195
Bondi H., Hoyle F., 1944, MNRAS, 104, 273
Booth C. M., Schaye J., 2009, MNRAS, 398, 53
Bouche N., Hohensee W., Vargas R., Kacprzak G. G., Martin C. L., Cooke J., Churchill C. W., 2012, MNRAS, 426, 801
Bower R. G., Benson A. J., Malbon R., Helly J. C., Frenk C. S., Baugh C. M., Cole S., Lacey C. G., 2006, MNRAS, 370, 645
Carilli C. L., Walter F., 2013, ARA&A, 51, 105
Carnall A. C. et al., 2015, MNRAS, 451, L16
Chabrier G., 2003, PASP, 115, 763
Chambers K. C., Miley G. K., van Breugel W., 1987, Nature, 329, 604
Chartas G., Brandt W. N., Gallagher S. C., 2003, ApJ, 595, 85
Cicone C. et al., 2014, A&A, 562, A21
Cicone C. et al., 2015, A&A, 574, A14
Cimatti A. et al., 2004, Nature, 430, 184
Costa T., Sijacki D., Trenti M., Haehnelt M. G., 2014, MNRAS, 439, 2146
Costa T., Sijacki D., Haehnelt M. G., 2015, MNRAS, 448, L30
Crenshaw D. M., Kraemer S. B., George I. M., 2003, ARA&A, 41, 117
Cresci G. et al., 2015, A&A, 582, A63
Croton D. J. et al., 2006, MNRAS, 365, 11
Dasyra K. M., Bostrom A. C., Combes F., Vlahakis N., 2015, ApJ, 815, 34
De Rosa G. et al., 2014, ApJ, 790, 145
De Young D. S., 1989, ApJ, 342, L59
Di Matteo T., Springel V., Hernquist L., 2005, Nature, 433, 604
Di Matteo T., Colberg J., Springel V., Hernquist L., Sijacki D., 2008, ApJ, 676, 33
Di Matteo T., Khandai N., DeGraf C., Feng Y., Croft R. A. C., Lopez J., Springel V., 2012, ApJ, 745, L29
Dijkstra M., Haiman Z., Mesinger A., Wyithe J. S. B., 2008, MNRAS, 391, 1961
Dubois Y., Devriendt J., Slyz A., Teyssier R., 2010, MNRAS, 409, 985
Dubois Y., Pichon C., Devriendt J., Silk J., Haehnelt M., Kimm T., Slyz A., 2013, MNRAS, 428, 2885
Everett J. E., 2007, Ap&SS, 311, 269
Fabian A. C., 2012, ARA&A, 50, 455
Fan X., 2006, New Astron. Rev., 50, 665
Ferland G. J., Korista K. T., Verner D. A., Ferguson J. W., Kingdon J. B., Verner E. M., 1998, PASP, 110, 761
Ferrara A., Scannapieco E., 2016, ApJ, 833, 46
Ferrarese L., Ford H., 2005, Space Sci. Rev., 116, 523
Feruglio C. et al., 2015, A&A, 583, A99
Gallerani S., Ferrara A., Neri R., Maiolino R., 2014, MNRAS, 445, 2848
Gallerani S., Fan X., Maiolino R., Pacucci F., 2017, Publ. Astron. Soc. Aust., 34, e022
Gebhardt K. et al., 2000, ApJ, 539, L13
Governato F., Colpi M., Maraschi L., 1994, MNRAS, 271, 317
Granato G. L., De Zotti G., Silva L., Bressan A., Danese L., 2004, ApJ, 600, 580
Haardt F., Madau P., 2001, in: Neumann D. M., Van J. T. T., eds., XXXVIth Rencontres de Moriond, XXIst Moriond Astrophysics Meeting, 64
Hahn O., Abel T., 2011, MNRAS, 415, 2101
Hirschmann M., Dolag K., Saro A., Bachmann L., Borgani S., Burkert A., 2014, MNRAS, 442, 2304
Hoyle F., Lyttleton R. A., 1939, Proc. Camb. Phil. Soc., 35, 405
Inayoshi K., Omukai K., 2012, MNRAS, 422, 2539
Johansson P. H., Naab T., Burkert A., 2009, ApJ, 690, 802
Ju W., Greene J. E., Rafikov R. R., Bickerton S. J., Badenes C., 2013, ApJ, 777, 44
Kakkad D. et al., 2016, A&A, 592, A148
Katz N., Weinberg D. H., Hernquist L., 1996, ApJS, 105, 19
Kauffmann G., Haehnelt M., 2000, MNRAS, 311, 576
Khalatyan A., Cattaneo A., Schramm M., Gottlober S., Steinmetz M., Wisotzki L., 2008, MNRAS, 387, 13
King A., 2003, ApJ, 596, L27
Kormendy J., Richstone D., 1995, ARA&A, 33, 581
Krongold Y., Nicastro F., Elvis M., Brickhouse N., Binette L., Mathur S., Jimenez-Bailon E., 2007, ApJ, 659, 1022
Kurk J. D. et al., 2007, ApJ, 669, 32
Lanz L., Ogle P. M., Alatalo K., Appleton P. N., 2016, ApJ, 826, 29
Lyu J., Rieke G. H., Alberts S., 2016, ApJ, 816, 85
Magorrian J. et al., 1998, AJ, 115, 2285
Maiolino R. et al., 2005, A&A, 440, L51
Maiolino R. et al., 2012, MNRAS, 425, L66
Marconi A., Hunt L. K., 2003, ApJ, 589, L21
Martin C. L., 1999, ApJ, 513, 156
Matsumoto T., Nakauchi D., Ioka K., Heger A., Nakamura T., 2015, ApJ, 810, 64
Matsuoka Y. et al., 2016, ApJ, 828, 26
Mayer L., Kazantzidis S., Escala A., Callegari S., 2010, Nature, 466, 1082
Morganti R., Veilleux S., Oosterloo T., Teng S. H., Rupke D., 2016, A&A, 593, A30
Mortlock D. J. et al., 2011, Nature, 474, 616
Newman S. F. et al., 2012, ApJ, 752, 111
Ostriker J. P., Choi E., Ciotti L., Novak G. S., Proga D., 2010, ApJ, 722, 642
Pacucci F., Pallottini A., Ferrara A., Gallerani S., 2017, MNRAS, 468, L77
Padovani P., Matteucci F., 1993, ApJ, 416, 26
Pallottini A., Gallerani S., Ferrara A., Yue B., Vallini L., Maiolino R., Feruglio C., 2015, MNRAS, 453, 1898

Pallottini A., Ferrara A., Gallerani S., Vallini L., Maiolino R., Salvadori S., 2017, MNRAS, 465, 2540
Perna M. et al., 2015, A&A, 583, A72
Pettini M., Rix S. A., Steidel C. C., Adelberger K. L., Hunt M. P., Shapley A. E., 2002, ApJ, 569, 742
Planck Collaboration XIII, 2016, A&A, 594, A13
Ragone-Figueroa C., Granato G. L., Murante G., Borgani S., Cui W., 2013, MNRAS, 436, 1750
Ramirez J. M., 2008, A&A, 489, 57
Rasia E., Borgani S., Murante G., Planelles S., Beck A. M., Biffi V., Ragone-Figueroa C., Granato G. L., Steinborn L. K., Dolag K., 2015, ApJ, 813, L17
Rees M. J., 1984, ARA&A, 22, 471
Reichard T. A. et al., 2003, AJ, 126, 2594
Richardson M. L. A., Scannapieco E., Devriendt J., Slyz A., Thacker R. J., Dubois Y., Wurster J., Silk J., 2016, ApJ, 825, 83
Richstone D. et al., 1998, Nature, 395, A14
Riechers D. A. et al., 2009, ApJ, 703, 1338
Rupke D. S. N., Veilleux S., 2011, ApJ, 729, L27
Salpeter E. E., 1964, ApJ, 140, 796
Saracco P. et al., 2005, MNRAS, 357, L40
Sazonov S. Y., Ostriker J. P., Ciotti L., Sunyaev R. A., 2005, MNRAS, 358, 168
Scannapieco E., Silk J., Bouwens R., 2005, ApJ, 635, L13
Schawinski K. et al., 2006, Nature, 442, 888
Schaye J. et al., 2015, MNRAS, 446, 521
Shakura N. I., Sunyaev R. A., 1973, A&A, 24, 337
Shankar F., Salucci P., Granato G. L., De Zotti G., Danese L., 2004, MNRAS, 354, 1020
Shankar F., Lapi A., Salucci P., De Zotti G., Danese L., 2006, ApJ, 643, 14
Sijacki D., Springel V., Di Matteo T., Hernquist L., 2007, MNRAS, 380, 877
Sijacki D., Springel V., Haehnelt M. G., 2009, MNRAS, 400, 100
Silk J., 2005, MNRAS, 364, 1337
Silk J., Mamon G. A., 2012, Res. Astron. Astrophys., 12, 917
Silk J., Rees M. J., 1998, A&A, 331, L1
Smith A., Bromm V., Loeb A., 2016, MNRAS, 460, 3143
Somerville R. S., Hopkins P. F., Cox T. J., Robertson B. E., Hernquist L., 2008, MNRAS, 391, 481
Springel V., 2005, MNRAS, 364, 1105
Springel V., Hernquist L., 2003, MNRAS, 339, 289
Springel V., Di Matteo T., Hernquist L., 2005, MNRAS, 361, 776
Stefan I. I. et al., 2015, MNRAS, 451, 1713
Sturm E. et al., 2011, ApJ, 733, L16
Talia M. et al., 2017, MNRAS, 471, 4527
Tanaka T. L., Li M., 2014, MNRAS, 439, 1092
Tescari E., Viel M., D'Odorico V., Cristiani S., Calura F., Borgani S., Tornatore L., 2011, MNRAS, 411, 826
Thielemann F.-K. et al., 2003, Nucl. Phys. A, 718, 139
Tombesi F., Cappi M., Reeves J. N., Nemmen R. S., Braito V., Gaspari M., Reynolds C. S., 2013, MNRAS, 430, 1102
Tombesi F., Melendez M., Veilleux S., Reeves J. N., Gonzalez-Alfonso E., Reynolds C. S., 2015, Nature, 519, 436
Tornatore L., Borgani S., Dolag K., Matteucci F., 2007, MNRAS, 382, 1050
Trakhtenbrot B., Lira P., Netzer H., Cicone C., Maiolino R., Shemmer O., 2017, ApJ, 836, 8
Tremmel M., Governato F., Volonteri M., Quinn T. R., 2015, MNRAS, 451, 1868
Tremmel M., Karcher M., Governato F., Volonteri M., Quinn T., Pontzen A., Anderson L., Bellovary J., 2017, MNRAS, 470, 1121
Valiante R., Schneider R., Maiolino R., Salvadori S., Bianchi S., 2012, MNRAS, 427, L60
Valiante R., Schneider R., Salvadori S., Gallerani S., 2014, MNRAS, 444, 2442
Vallini L., Gallerani S., Ferrara A., Pallottini A., Yue B., 2015, ApJ, 813, 36
van de Voort F., Schaye J., Booth C. M., Dalla Vecchia C., 2011, MNRAS, 415, 2782
van den Hoek L. B., Groenewegen M. A. T., 1997, A&AS, 123, 305
Venemans B. P. et al., 2013, ApJ, 779, 24
Venemans B. P., Walter F., Zschaechner L., Decarli R., De Rosa G., Findlay J. R., McMahon R. G., Sutherland W. J., 2016, ApJ, 816, 37
Wagner A. Y., Umemura M., Bicknell G. V., 2013, ApJ, 763, L18
Walter F., Carilli C., Bertoldi F., Menten K., Cox P., Lo K. Y., Fan X., Strauss M. A., 2004, ApJ, 615, L17
Walter F., Riechers D., Cox P., Neri R., Carilli C., Bertoldi F., Weiss A., Maiolino R., 2009, Nature, 457, 699
Wang R. et al., 2010, ApJ, 714, 699
Wang R. et al., 2016, ApJ, 830, 53
Wang J.-M., Chen Y.-M., Yan C.-S., Hu C., Bian W.-H., 2007, ApJ, 661, L143
Waters D., Di Matteo T., Feng Y., Wilkins S. M., Croft R. A. C., 2016, MNRAS, 463, 3520
Whitaker K. E. et al., 2013, ApJ, 770, L39
Wiersma R. P. C., Schaye J., Smith B. D., 2009, MNRAS, 393, 99
Williams R. J., Maiolino R., Krongold Y., Carniani S., Cresci G., Mannucci F., Marconi A., 2017, MNRAS, 467, 3399
Willott C. J., McLure R. J., Jarvis M. J., 2003, ApJ, 587, L15
Willott C. J., Bergeron J., Omont A., 2015, ApJ, 801, 123
Woosley S. E., Weaver T. A., 1995, ApJS, 101, 181
Wu X.-B. et al., 2015, Nature, 518, 512
Wurster J., Thacker R. J., 2013, MNRAS, 431, 2513
Zinn P.-C., Middelberg E., Norris R. P., Dettmar R.-J., 2013, ApJ, 774, 66
Zubovas K., Nayakshin S., King A., Wilkinson M., 2013, MNRAS, 433, 3079

APPENDIX

In our implementation of BH kinetic feedback (Section 2.3), all the ∼200 neighbouring gas particles lying within the bi-cone or sphere have the same probability to be kicked (equation 10). This could potentially cause a problem as gas particles can be kicked and AGN wind can be launched far from the BH itself. The problem will cause the BH to clear out gas around it, and the radius of influence of the BH (its smoothing length) would grow artificially large.

We checked that there is no unphysical behaviour of the BH smoothing length ($h_{\rm BH}$) because of our adopted numerical prescription. Therefore, the potential problem does not occur. The number of gas particles actually kicked by a BH at a time-step is just a few (maximum 5 to 6) in our simulations.

The redshift evolution of the BH smoothing length (equation 9) of the most-massive BH in the three AGN runs is plotted in Fig. A1, right-hand panel. These are the same BHs whose mass versus redshift are plotted in Fig. 2. For comparison, the horizontal dashed line indicates the gravitational softening length ($L_{\rm soft} = 1\,h^{-1}\,{\rm kpc}^{-1}$ comoving) for the high-resolution DM and gas particles.

Fig. A1 demonstrates that $h_{\rm BH}$ depends dominantly (and inversely) on the density of gas where the BH lies. Gas density at galaxy centres becomes higher with time. Therefore, as galaxy-central BHs grow more massive with time, they have a smaller $h_{\rm BH}$. There is no abnormal increase of $h_{\rm BH}$, which looks to have an expected evolution. We see that $h_{\rm BH} \sim L_{\rm soft}$ for most of the time, over redshifts $z = 9$–6, when the BHs have the highest growth.

At $z > 9$, $h_{\rm BH}$ of the galaxy-central BHs goes up to a maximum $\sim 3L_{\rm soft}$. At such early epochs, there is the possibility to apply a kind of distance-weighted, or density-dependent expression for the probability that a gas particle is kicked (such that the closest gas particles having the highest probability to be ejected). Such alternative numerical implementation are however beyond the goals of the current work, and deferred to future studies. At the present state, it is unclear if and how the choice of distance and density dependence of the kicking probability can affect the resulting feedback. Further (and preferably higher resolution) simulations are required to perform a dedicated study on the numerical aspects.

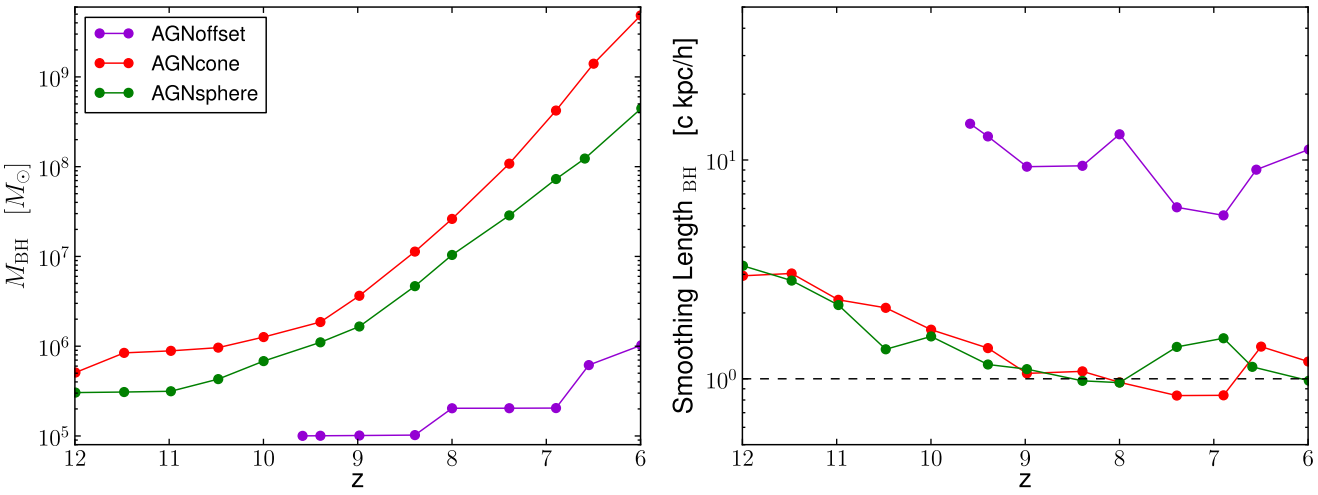

Figure A1. Evolution with redshift of BH mass (left-hand panel) and BH smoothing length (right) of the most-massive BH in each run. These are the same BHs which were plotted in Fig. 2. The different colours discriminate the runs as labelled in the left-hand panel. The horizontal dashed line in the right-hand panel indicates the gravitational softening length for the high-resolution DM and gas particles.

This paper has been typeset from a TEX/LATEX file prepared by the author.